


# High-field Characterization of Piezoelectric and Magnetostrictive Actuators

RADU POMIRLEANU AND VICTOR GIURGIUTIU\*

*Department of Mechanical Engineering, University of South Carolina, Columbia, SC 29208*

**ABSTRACT:** High-field theoretical and experimental analysis of piezoelectric and magnetostrictive actuators is presented. First, the analysis of a piezoelectric stack actuator (PiezoSystems Jena PAHL 120/20) is described. A theoretical model based on the linear theory of piezoelectricity is developed. Extensive experiments were conducted, aimed at low-frequency dynamic electro-mechanical behavior characterization. Curve fitting procedures are used to adjust the model coefficients for various load levels. Through comparison with experimental data, the model is adjusted to include nonlinear terms related to higher losses on the unloading cycle. Second, the impedance analysis of a magnetostrictive actuator (Etrema AA140J025) is described. Linear piezomagnetism is assumed, as an approximation to nonlinear magnetostrictive behavior about a bias point. Low-field and high-field impedance measurements were performed, revealing left shifting of the actuator resonance as the power is increased. Model tuning of the impedance model on the experimental data showed material parameters trends similar with those reported in the literature. Although the numerical values developed during this phenomenological study are particular for the actuators under consideration, the characterization approach can be extended to analysis of other actuators of this type.

Key Words: Author please provide Keywords ?? 

## INTRODUCTION

ACTIVE-MATERIALS technology offers direct conversion of electrical energy to high-frequency linear motion. High-performance solid-state induced-strain actuators (piezoelectric, electrostrictive, or magnetostrictive) have large power densities and relatively large forces at up to 0.1%. The opportunity for direct electrical-to-mechanical energy conversion is welcomed in a number of applications including vibration reduction, active aeroelastic control, etc. Induced-strain actuators are basically of two types:

- **Electroactive**, such that an induced strain is generated by the application of an electric field. Piezoelectric (e.g., PZT) and electrostrictive (e.g., PMN) ceramics are commonly used for electroactive high-power actuators
- **Magnetoactive**, in which the induced strain is generated by the application of a magnetic field. Magnetostrictive alloys (e.g., Terfenol-D) are commonly used in magnetoactive high-power actuators.

These two active-material types have different but complementary characteristics. On one hand, the electroactive materials require high electric fields,

which can be produced by applying relatively large voltages across very thin wafers. For this reason, practical electroactive material actuators are built in stacks, commonly known as *piezostacks*. Electroactive materials also have very large dielectric permittivity, and the resulting stacks have fairly large electric capacitance. When electroactive actuators are operated in dynamic regime, very large reactive powers are encountered, of the order of  $i\omega CV^2$ . Under constant voltage operation, the reactive power of electroactive actuators increases linearly with frequency. On the other hand, the magnetoactive materials require high magnetic fields, which can be produced by applying relatively large currents through a multiturn coil. The resulting magnetic field increases proportionally with both the current and the number of turns in the coil. When magnetoactive actuators are operated in dynamic regime, very large reactive powers are also encountered, of the order of  $V^2/(i\omega L)$ . Under constant voltage operation, the reactive power of magnetostrictive actuators decreases with frequency as  $1/\omega$ . Based on the reactive power requirements under constant voltage operation, it seems that piezoelectric devices are easier to use at low frequencies, while the magnetostrictive devices are easier to use at high frequencies. However, in several dynamic applications, the frequency is neither high frequency, nor low frequency. For these applications,

\*Author to whom correspondence should be addressed.  
E-mail: victorg@sc.edu

both electroactive and magnetostrictive actuators have been proposed. It is apparent that, for an informed design decision, the properties and behavior of both types of solid-state actuators must be well understood. This paper describes an effort to comparatively evaluate two commercially available high-power solid-state actuators, one a piezostack, the other a magnetostrictive device. Phenomenological modeling was developed and experimental tests were performed to calibrate and adjust the model. In the end, a curve-fitting approach was used to accommodate the nonlinearities present at high-power regimes. During the experiments, certain equipment limitations were encountered, such that the piezostack could only be tested up to 5 Hz, while the magnetostrictive device could only be tested over 1 kHz. In spite of these limitations, we believe that the modeling and experimental results given in this paper will be found useful in the design of induced-strain actuation application utilizing electroactive and magnetostrictive solid-state actuators.

## STATE OF THE ART IN ACTIVE MATERIAL ACTUATORS MODELING AND CHARACTERIZATION

### Piezoelectric Stack Actuators

Krueger and Berlincourt (1961) characterized the nonlinear behavior of piezoelectric materials under high-stress conditions by relating the deviations from linear behavior to macroscopic quantities such as dielectric permittivity, piezoelectric coefficient, loss factor, and coupling coefficients. The basic differences between hard and soft PZTs were recognized, reflected in the different material coefficients dependence on load conditions. Material properties were found to vary with the electro-mechanical boundary conditions, as well as time-history. The dependence of dielectric permittivity on the applied stress and electric field was also observed (Krueger, 1967, 1968; Brennan and McGowan, 1997; Jordan et al., 2000). Experiments on doped PZT ceramics were pursued to determine the polarization domain switching under high electric fields and compressive stresses in order to explain the nonlinear effects (Lynch, 1996, Zhang et al., 1997; Fan et al., 1999; Ching-Yu and Hagood, 2000; Lin and Hagood, 2000; Yang et al., 2000).

Modeling efforts tried to bridge the gap between the micromechanics of the crystal structure and the macroscopic properties of piezoceramics under high electro-mechanical conditions (Chen et al., 1997; Fan et al., 1999; Hwang and McMeeking, 2000; Huber and Fleck, 2001). Chaplya and Carman (2001, 2002) characterized the piezoelectric domain switching using macroscopic quantities through a law of mixtures. Such

efforts have been confined to the analysis of bulk piezoelectric material subjected to precisely-known electro-mechanical excitation, and under negligible boundaries conditions influence. However, stacked piezoelectric actuators consist of hundreds of thin layers, and the electro-mechanical boundary conditions for every layer are insufficiently known and difficult to define. While the extensive analysis of a single piezoceramic layer was accomplished through the study of the sheet actuators using either the 31 or the 33 effect (e.g. Yoshikawa et al., 1999; Sirohi and Chopra, 2000), the characterization of actual stack actuators has been, so far, phenomenological, in order to obtain essential design information about the mechanical stiffness, energy density, load amplitude, temperature effects, and durability (Straub and Merkle, 1995; Lee and Chopra, 1999; Mitrovic et al., 2000, 2001; Pan et al., 2000; Straub et al., 2001). These tests used various methods for the application of the mechanical load: dead weight (Lee and Chopra, 1999), MTS machine (Mitrovic et al., 2000, 2001), variable impedance by the means of a variable stiffness spring (Straub et al., 2001), and constant stiffness spring mounted in series with the smart material actuator (Pan et al., 2000).

### Magnetostrictive Actuators

Magnetostrictive materials expand in the presence of a magnetic field, as their magnetic domains align with the field. Terbium-based compounds, such as the commercially available Terfenol-D ( $Tb_xDy_{1-x}Fe_{2-y}$ , with  $0.27 \leq x \leq 0.3$ , and  $0 \leq y \leq 0.1$ ), show magnetostriction of up to 2000  $\mu$ strain at temperatures up to 80°C and higher, with significantly nonlinear and hysteretic behavior. Magnetostriction is dependent on the applied stress, since the magnetic domains tend to align perpendicularly to the direction of applied stress in the absence of any applied magnetic field.

Early experimental studies of magnetostrictive materials showed them to be strongly nonlinear and hysteretic (Clark, 1993). This behavior is related to magnetic anisotropy, magneto-mechanical coupling, and magnetization saturation (Engdahl, 2000). The material behavior complexity is increased by the easy growth in the nonprincipal crystallographic [112] direction, commonly used for actuators manufacturing, and the dendritic sheets twinning (Clark, 1993).

While the linear approximation is strictly valid for small excitations, it becomes a useful tool when it models magnetically biased magnetostrictive materials, provided the saturation magnetization is not reached within the operational range (Hall and Flatau, 1995; Ackerman et al., 1996; Engdahl, 2000). The active material modeled this way is termed piezomagnetic. This approach is largely used when the nonlinear

magnetostrictive behavior is characterized empirically (Faidley et al., 1998, 2001; Kellogg and Flatau, 2001).

Describing magnetically unbiased transducers requires nonlinear modeling, which comes at the cost of implementing numerical solutions of the time-domain behavior (Calkins et al., 1997; Smith, 1998). These one-dimensional nonlinear models employing the physics of ferromagnetism have been successfully developed and tested against experimental data at low frequencies (Calkins et al., 1997). Another approach to writing nonlinear constitutive equations for the magnetostrictive material is to retain more than the first terms from the series expansion of the magneto-elastic Gibbs free energy (Carman and Mitrovic, 1995), using a parabolic approximation for the strain dependence on the magnetic field. Through finite element solving techniques, this approach is able to capture the magnetostrictive behavior from zero to approximately 75% of the saturation-driving fields for a large range of stresses, less the magnetostriction saturation occurring at higher fields. Carman and Mitrovic (1995) showed that this nonlinear model needs only a constant coupling coefficient at the expense of a strong variation of the compliance coefficient. This numerically efficient approach was implemented for magnetically unbiased magnetostrictive actuator operation (Pratt et al., 1999).

### MODELING OF PIEZOELECTRIC STACK ACTUATOR

The PiezoSystems Jena piezoelectric actuator PAHL 120/20 (Figure 1(a)) consists of an active material stack prestressed to  $F_0 = 350$  N by an internal spring inside a steel casing (Figure 1(b)). The mechanical prestress is needed to prevent tensile stresses in the stack during

static and dynamic applications. The space between the steel casing and the piezoelectric stack is filled with epoxy resin to protect the stack from shocks. The piezoelectric stack transmits force through a steel push-rod. The piezoelectric material used is a soft PZT, with the manufacturer provided characteristics shown in Table 1.

The linear piezoelectric material modeling (ANSI/IEEE Std. 176/1987) assumes constitutive equations in terms of three material-properties tensors (compliance,  $s_{ijkl}$ , piezoelectric,  $d_{ijk}$ , and dielectric permittivity,  $\epsilon_{ij}$ ) and four field variables (strain,  $S_{ij}$ , stress,  $T_{kl}$ , electric field,  $E_k$ , and electric displacement,  $D_i$ ):

$$S_{ij} = s_{ijkl}^{(E)} T_{kl} + d_{kij} E_k \quad D_i = d_{ikl} T_{kl} + \epsilon_{ik}^{(T)} E_k \quad (1)$$

However, full-power operation is nonlinear, and the linear equations are only a first order approximation.

**Table 1. PiezoSystems Jena actuator properties.**

Actuator Properties and Dimensions	
Maximum displacement ( $\mu\text{m}$ )	120
Voltage range (V)	-10 to 150
Actuator internal stiffness (kN/mm)	30
Maximum tensile force (N)	350
Maximum blocked force (N)	3500
Capacitance (for small strength electrical fields) ( $\mu\text{F}$ )	42
Resonance frequency (kHz)	5
Length (mm)	126
Diameter (mm)	20
Piezoelectric coefficient $d_{33}$ ( $10^{-12} \times \text{m/V}$ )	700
Compliance $s_{33}^E$ ( $10^{-12} \times \text{m}^2/\text{N}$ )	20.8
Coupling factor $\kappa_{33}$	0.65
Stack length $L$ (mm)	118
Stack area $A$ ( $\text{mm}^2$ )	64
Layer thickness $t$ (mm)	0.1

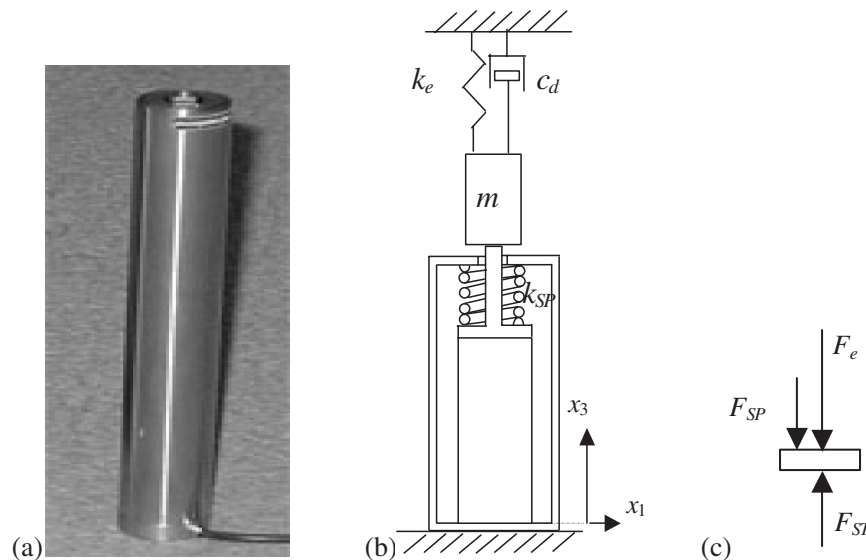


**Figure 1.** (a) Piezoelectric stack actuator PAHL 120/20; (b) idealized actuator and external structure; (c) free-body diagram for the pushing rod.

One way to utilize linear equations for modeling full-stroke nonlinear behavior is to consider that the material tensors  $s_{ijkl}$ ,  $d_{ijk}$ , and  $\varepsilon_{ij}$  vary with electro-mechanical load. The linear piezoelectric equations were simplified to the case where only the 3-direction effects (i.e. in the direction of remnant polarization) are retained. In contracted Voigt notation,

$$S_3 = s_{33}^{(E)} T_3 + d_{33} E_3 \quad D_3 = d_{33} T_3 + \varepsilon_3^{(T)} E_3 \quad (2)$$

The dynamic response under in-phase electro-mechanical loading may be modeled using the 1-D wave equation (Ikeda, 1999; Giurgiutiu, 1996) of an elastic continuum:

$$\rho \frac{\partial^2 u_3}{\partial \tau^2} = \frac{\partial T_3}{\partial x_3} \quad (3)$$

The stress gradient in the  $x_3$  direction can be further expressed as:

$$\begin{aligned} \frac{\partial T_3}{\partial x_3} &= \frac{\partial}{\partial x_3} \left( \frac{1}{s_{33}^{(E)}} S_3 - \frac{d_{33}}{s_{33}^{(E)}} E_3 \right) \\ &= \frac{\partial}{\partial x_3} \left( \frac{1}{s_{33}^{(E)}} S_3 - \frac{d_{33}}{s_{33}^{(E)}} \left( \frac{1}{\varepsilon_{33}^{(T)}} D_3 - \frac{d_{33}}{\varepsilon_{33}^{(T)}} T_3 \right) \right) \\ &= \frac{1}{s_{33}^{(E)}} \frac{\partial S_3}{\partial x_3} + \frac{d_{33}^2}{s_{33}^{(E)} \varepsilon_{33}^{(T)}} \frac{\partial T_3}{\partial x_3} - \frac{d_{33}}{s_{33}^{(E)} \varepsilon_{33}^{(T)}} \frac{\partial D_3}{\partial x_3} \end{aligned} \quad (4)$$

Since  $\nabla \cdot \mathbf{D} \cong \partial D_3 / \partial x_3 = 0$  inside the active material, we have

$$\begin{aligned} \frac{\partial T_3}{\partial x_3} &= \frac{1}{s_{33}^{(E)} \left( 1 - \left( \frac{d_{33}^2}{s_{33}^{(E)} \varepsilon_{33}^{(T)}} \right) \right)} \frac{\partial S_3}{\partial x_3} \\ &= \frac{1}{s_{33}^{(E)} (1 - \kappa_{33}^2)} \frac{\partial^2 u_3}{\partial x_3^2} = \frac{1}{s_{33}^{(D)}} \frac{\partial^2 u_3}{\partial x_3^2} \end{aligned} \quad (5)$$

The wave equation becomes:

$$\frac{\partial^2 u}{\partial \tau^2} = c^2 \frac{\partial^2 u}{\partial x_3^2}, \quad \text{with } c^2 = \frac{1}{\rho \cdot s_{33}^{(D)} (1 - i\eta)} \quad (6)$$

The parameter  $\eta$  accounts for mechanical losses, including material damping, losses in the bonding between electrodes and piezo-material, and losses in the surrounding resin. Consequently, we introduce the effective complex compliance  $s_{33}^* = s_{33} (1 - i\eta)$ . The excitation voltage is assumed to consist of superposed DC and AC components, i.e.:

$$v(\tau) = V_0 + V_a e^{i\omega\tau} \quad (7)$$

where  $V_0$  and  $V_a$  are the DC bias and the AC amplitude, respectively. The boundary conditions associated with Equation (6) are:

$$u(x_3 = 0, \tau) = 0, \quad \text{and } A \cdot T_3(x_3 = L, \tau) = F_{ST}(\tau) \quad (8)$$

where  $F_{ST}(\tau)$  is the force in the piezo-stack,  $F_{ST}(\tau) = F_b + F_a(\tau)$ . The bias force  $F_b$  consists of the internal-spring prestress,  $F_0$ , external preload,  $F_e$ , and response to the bias voltage,  $V_0$ . Denote  $\gamma = \omega/c$  and assume a displacement solution of the form:

$$u(x_3, \tau) = (C_1 \sin(\gamma x_3) + C_2 \cos(\gamma x_3)) e^{i\omega\tau} - C_3 x_3 \quad (9)$$

At  $x_3 = 0$ ,  $C_2 e^{i\omega\tau} = 0, \forall \tau$ . Hence,  $C_2 = 0$ . At  $x_3 = L$ ,  $S_3(x_3 = L, \tau) = \gamma C_1 \cos(\gamma L) e^{i\omega\tau} - C_3$ , and hence Equations (2), (8), and (9) yield:

$$\begin{aligned} C_1 &= \frac{d_{33}^* V_a}{t} \left( \gamma \cos(\gamma L) + \frac{s_{33}^*}{A} k_D(\omega) \sin(\gamma L) \right)^{-1}, \\ C_3 &= - \left( \frac{s_{33}^*}{A} F_b + \frac{d_{33}^*}{t} V_0 \right) \end{aligned} \quad (10)$$

where  $d_{33}^* = d_{33} (1 - i\lambda)$ , to account for imperfect piezoelectric energy conversion (Holland, 1967), and the dynamic stiffness of the structure outside the stack represented as a one degree-of-freedom spring-mass-damper system (Figure 1(b)), is:

$$k_d(\omega) = m(\omega_n^2 - \omega^2) + i\omega c_d \quad \text{with } \omega_n = \left( \frac{k_e + k_{SP}}{m} \right)^{1/2} \quad (11)$$

Hence,

$$\begin{aligned} u(x_3, t) &= \frac{d_{33}^* V_a e^{i\omega\tau}}{t} \left( 1 + \frac{s_{33}^* k_D(\omega)}{A \gamma} \tan(\gamma L) \right)^{-1} \frac{\sin(\gamma x)}{\gamma \cos(\gamma L)} \\ &\quad + x_3 \left[ \frac{s_{33}^*}{A} \left( F_0 + F_e^{(b)} \frac{k_{ST}^*}{k_{ST}^* + k_{SP}} \right) \right. \\ &\quad \left. + \frac{d_{33}^*}{t} V_0 \frac{k_{ST}^*}{k_e + k_{SP} + k_{ST}^*} \right] \end{aligned} \quad (12)$$

Hence, the actuator stroke,  $u_{ST} = u(x_3 = L, \tau)$ , becomes:

$$\begin{aligned} u_{ST}(\tau) &= \frac{d_{33}^* V_a \tan(\gamma L) e^{i\omega\tau}}{t \gamma (1 + (s_{33}^*/A)(k_d(\omega)/\gamma) \tan(\gamma L))} \\ &\quad + \frac{F_e^{(b)}}{k_{ST}^* + k_{sp}} + \frac{L}{t} d_{33}^* V_0 \frac{k_{ST}^*}{k_{ST}^* + k_{SP} + k_e} \end{aligned} \quad (13)$$

Using Equation (13) in Equation (2), and recalling  $F_{ST}(\tau) = A \cdot T_3(x_3 = L, \tau)$ , yields:

$$\begin{aligned} F_{ST}(\tau) = & -F_{\text{block}} \frac{V_a}{V_0} e^{i\omega\tau} \left( 1 + \frac{s_{33}^* k_d(\omega)}{A \gamma} \tan(\gamma L) \right)^{-1} \\ & + F_0 + F_e^{(b)} \frac{k_{ST}^*}{k_{ST}^* + k_{SP}} \\ & + F_{\text{block}} \left( \frac{k_e + k_{SP}}{k_e + k_{SP} + k_{ST}^*} + \frac{V_a}{V_0} e^{i\omega\tau} \right) \end{aligned} \quad (14)$$

where the static blocked force corresponding to the bias voltage,  $V_0$ , is:

$$F_{\text{block}} = -\frac{d_{33}^* A}{s_{33}^* t} V_0 \quad (15)$$

The external force is given by (Figure 1(c)):

$$F_e(\tau) = F_{ST}(\tau) - k_{SP} u_{ST}(\tau) - F_0 \quad (16)$$

To model the electric current, the second part of Equation (2) is written as:

$$D_3 = d_{33}^* \frac{F_{ST}(\tau)}{A} + \frac{\varepsilon_{33}^*}{t} (V_0 + V_a e^{i\omega\tau}) \quad (17)$$

where electric losses were modeled as  $\varepsilon_{33}^* = \varepsilon_{33}(1 - i\delta)$ . The electric displacement  $\mathbf{D}$  is related to the free charge distribution,  $q$ , by the equation  $\text{div } \mathbf{D} = q$  (Maxwell, 1891). For one-dimensional geometry, this equation integrates to  $Q = D_3 A$ , where  $Q$  is the free charge accumulated on the electrodes. The instantaneous current is the time derivative of the free charge, i.e.,

$$\begin{aligned} i_{ST}(\tau) = & \frac{dQ}{d\tau} = \frac{L}{t} i\omega V_a e^{i\omega\tau} \\ & \times \left[ d_{33}^* F_{\text{block}} \left( \left( 1 + \frac{s_{33}^* k_d(\omega)}{A \gamma} \tan(\gamma L) \right)^{-1} - 1 \right) + \frac{\varepsilon_{33}^* A}{t} \right] \end{aligned} \quad (18)$$

The instantaneous power is given by  $p(\tau) = i_{ST}(\tau) \cdot v(\tau)$ . The average active power per cycle,  $P_a$ , can then be calculated as:

$$P_a = f \cdot \int_{\text{cycle}} \text{Re}(p(\tau)) d\tau = f \cdot \int_0^{1/f} \text{Re}(v(\tau) \cdot i_{ST}(\tau)) d\tau \quad (19)$$

## TESTING OF THE PIEZOELECTRIC STACK ACTUATOR

Experiments were performed to evaluate the blocked force, the characteristic loops, and the mechanical and electrical envelopes of the piezoelectric stack actuator


PAHL 120/20, in quasi-static and low-frequency dynamic regimes. The characteristic loops are the force–displacement, current–voltage, and voltage–displacement curves. The mechanical envelope for a given frequency correlates the extreme values of voltage, displacement, and force and is a useful tool when determining the mechanical capabilities of the actuator. Likewise, the electrical envelope correlates force and voltage with the peak power and the active average power per cycle, respectively, providing a generic picture of the actuator power requirements and losses.

## Experimental Setup

The experimental setup is shown in Figure 2(a). The signal generated by a Hewlett Packard HP 3312A function generator was amplified by a high-voltage 2-channel TREK 750/50 amplifier, and sent to the PAHL 120/20 actuator. To increase the dynamic range, two channels of the TREK 750/50 amplifier were merged. The amplified signal was tapped to the HP5460B digital oscilloscope. A parallel circuit consisting of a 1 k $\Omega$  resistor and a normally open switch was used for discharging the stack. The current going through the actuator was measured using the voltage drop across a calibrated 1  $\Omega$  resistor placed in series with the actuator. This signal was passed through a low-pass filter and displayed on the second channel of the HP5460B. The external load was applied using a LongYear compression frame and a proving ring. The proving ring was equipped with a dial gage calibrated to measure force (accuracy  $\pm 7.2$  N) (Figure 2(b)) and four strain gages in full bridge configuration. The strain gage signal was passed through a low-pass filter and displayed on a TDS210 digital oscilloscope. The displacement of the actuator was measured with a Philtec D100 optical displacement transducer and sent to the other channel of the Tektronix TDS210 oscilloscope (Figure 2(c)). The 4 waveforms captured on the digital oscilloscopes were downloaded to a PC.

## Measurements Procedures and Results

### MEASUREMENTS OF THE BLOCKED FORCE

The blocked force is defined as the force developed in the actuator when pushing against a body of infinite stiffness, such that there is no external displacement, all the induced strain being consumed internally. Since the achievement of infinite stiffness is impractical, three methods were devised to attain the condition of zero external displacement under static loading 

- (a) Static Method 1: Apply a given voltage, thus expanding the stack, and then compress the actuator until the net displacement is brought back to zero.

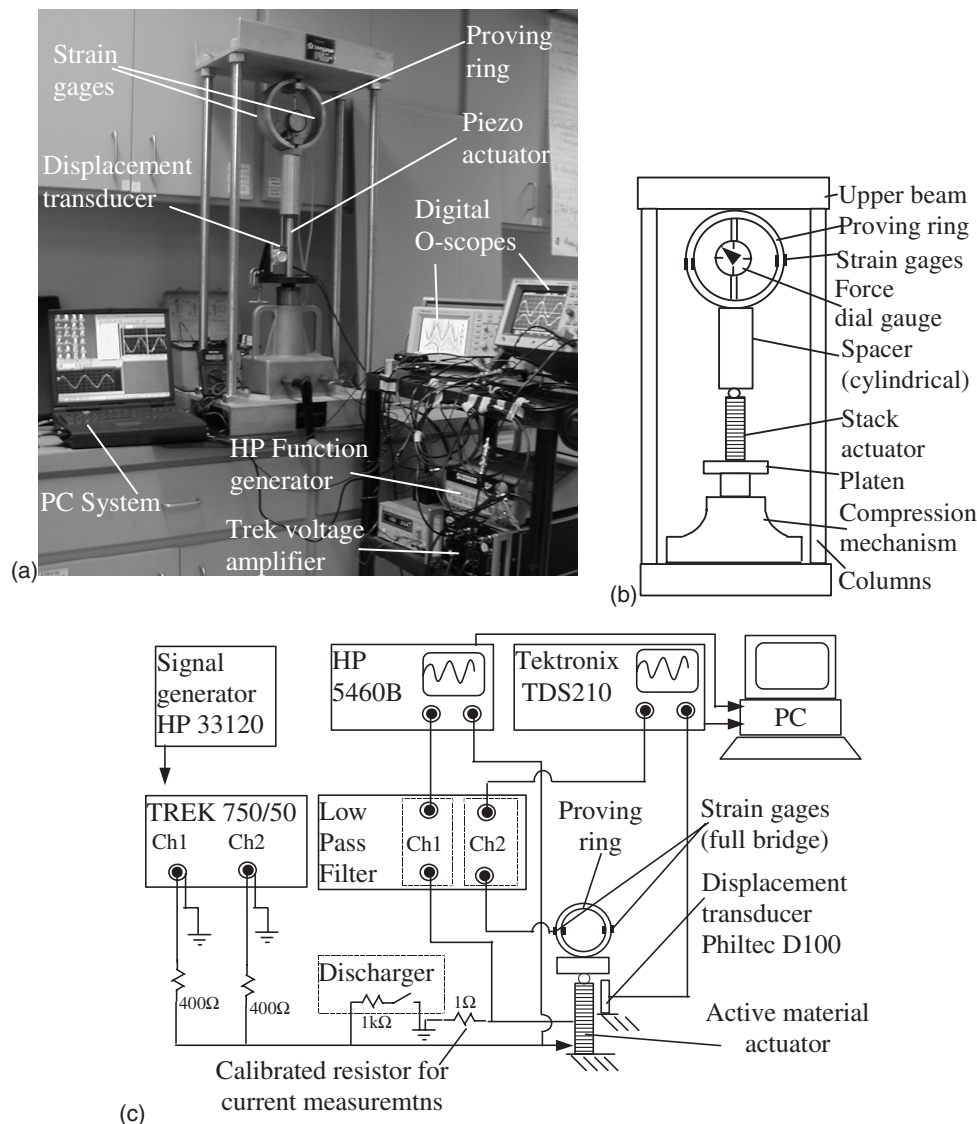


**Figure 2.** (a) Experimental setup for dynamic testing of PAHL 120/20; (b) schematic of the compression frame; (c) excitation and measurements diagram.

- (b) Static Method 2: Compresses the stack to a given force, and then adjusts the voltage until the initial length of the stack is recovered. Record the final voltage and force values.
- (c) Dynamic Method: Apply the voltage duty-cycle and then compress the assembly until the maximum value of the displacement waveform coincides with the zero voltage/zero force displacement signal, and record the blocked force value as the maximum of the force waveform.

The results of blocked force measurements for static and dynamic excitation are shown in Figure 3, with the theoretical line given by Equation (15) superposed. As seen from Figure 3, the linear theory over-predicts the quasi-static blocked force measurements, but seems to be a good approximation to the low-frequency dynamic blocked force measurements. Regarding the static data,

the two testing methods give similar results for low and moderate applied voltages. For high applied electric fields, the results of the two methods are shown to diverge.

#### STATIC CHARACTERIZATION

To completely describe the piezoelectric actuator behavior under static conditions, the actuator displacement under combined electro-mechanical load (force and voltage) had to be recorded. Due to the assumed spring-like character of the external load, distinction had to be made between the measurement procedures for the points situated above and respectively below the external stiffness line of Figure 4. For points situated above and on the external stiffness line, the actuator was first compressed against the proving ring until a given prestress level was attained, and then the voltage was applied. The load application rate was below 0.05 Hz.

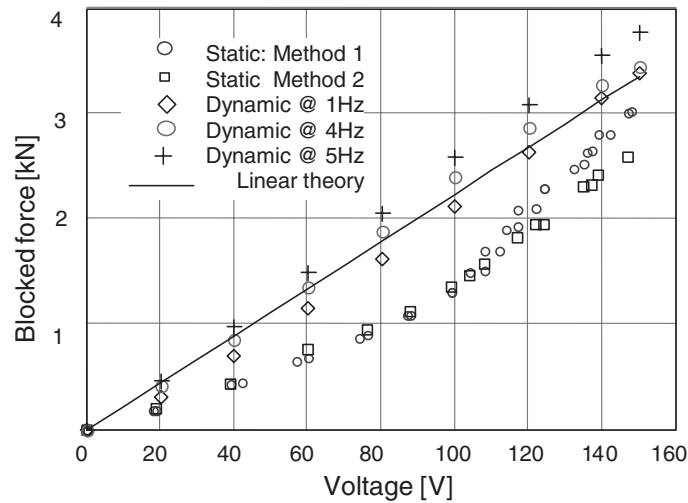


Figure 3. Blocked force variation with voltage: theory and experiment.

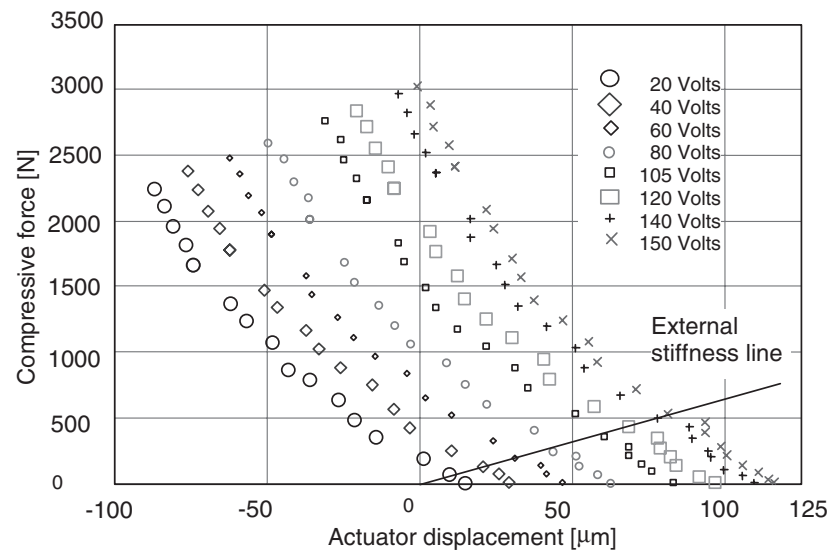


Figure 4. Force-displacement-voltage correlations.

Data points evaluated using this procedure lie on curves parallel to the external stiffness curve, and located above it. This procedure cannot be used for the points situated below the external stiffness line, because this would require placing the stack in tension. For points below the external stiffness line, the voltage was applied directly with the actuator resting against the proving ring. The data points evaluated with this procedure also lie on curves parallel to the external stiffness curve, but situated below it (Figure 4).

The interpolation of the curves for constant voltage of Figure 4 at zero displacement yield values consistent with the static blocked force values shown in Figure 3.

#### LOW-FREQUENCY DYNAMIC CHARACTERIZATION

The maximum frequency attained during the dynamic regime was  $f_c \approx 5$  Hz. For a capacitive load, the

maximum achievable frequency is limited by the maximum electric current capability of the power amplifier (Figure 5). Given the 0.1 A maximum current of the TREK 750/50 amplifier, a voltage duty-cycle of 0–150 V, and the PAHL 120/20 piezoelectric actuator capacitance of 42  $\mu$ F, a maximum frequency of 7.1 Hz is predicted. Experimental results showed that current saturation of the power supply started to appear at frequencies as low as 5 Hz, mainly due to electric permittivity dependence on the electro-mechanical loading. Hence, the highest testing frequency used was  $f_c = 5$  Hz.

The procedure for dynamic measurements resembles the procedure used for static measurements, with some modifications to account for the dynamic effects. The excitation voltage was of the form given in Equation (7), with  $V_a = V_0$ . The waveforms for each setting were captured and stored in a PC for further processing.

The dynamic data was complemented with no-load measurements of the piezoelectric actuator for each frequency. A test matrix covering four frequencies, eight voltages, and seven prestress conditions was used (Figure 6).

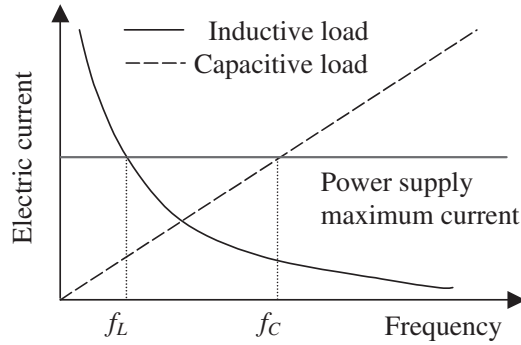


**Figure 5.** Power supply frequency restrictions for the operation of inductive and capacitive loads.

## DATA PROCESSING AND MODEL TUNING FOR THE PIEZOELECTRIC ACTUATOR

### Static Results

As shown in Figure 7, the piezoelectric linear static model predicts well at zero-load conditions, but it is a poor predictor at high-load conditions. We applied phenomenological coefficient tuning using a bivariate cubic regression of the actuator displacement (Figure 8):

$$u = C_0 F_e^3 + C_1 F_e^2 V + C_2 F_e V^2 + C_3 V^3 + C_4 F_e^2 + C_5 F_e V + C_6 V^2 + C_7 F_e + C_8 V \quad (20)$$

The force in the active material stack,  $F_{ST}$ , is expressed as the sum of the measured force and the force exerted by the prestress spring,  $k_{SP}$ . Upon substitution of  $F_{ST} = F_e + F_0 + k_{SP} \cdot u$  into Equation (14), we obtain the description of the overall actuator

Load case	Frequency=5Hz						No external load
	Frequency=4Hz						
	Frequency=2Hz						
Voltage range	Frequency=1Hz						
	Load: $k_e = 6.5 \cdot 10^6$ , $\omega_n = 450\text{Hz}$ , $\zeta = 0.05$ Pre-stress (N)						
	0	570	1150	1700	2300	2900	
0 – 20 V	✓	✓	✓	✓	✓	✓	✓
0 – 40 V	✓	✓	✓	✓	✓	✓	✓
0 – 60 V	✓	✓	✓	✓	✓	✓	✓
0 – 80 V	✓	✓	✓	✓	✓	✓	✓
0 – 100 V	✓	✓	✓	✓	✓	✓	✓
0 – 120 V	✓	✓	✓	✓	✓	✓	✓
0 – 140 V	✓	✓	✓	✓	✓	✓	✓
0 – 150 V	✓	✓	✓	✓	✓	✓	✓

**Figure 6.** Test matrix for dynamic measurement of the piezoelectric actuator PAHL 120/20.

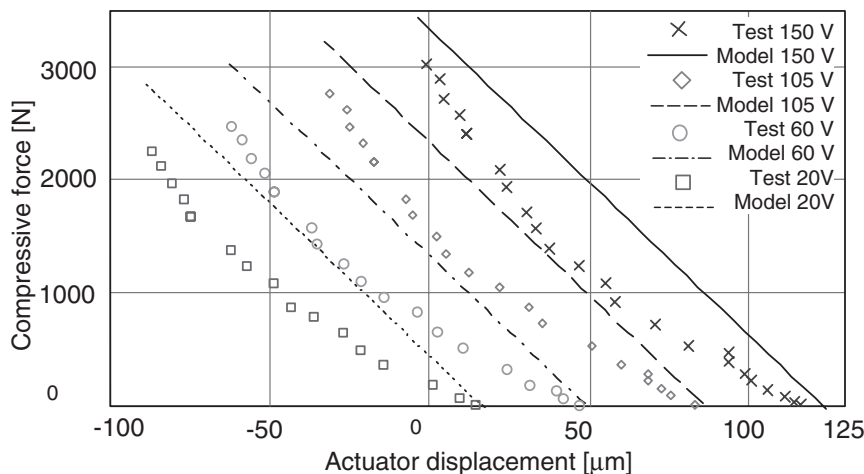


**Figure 7.** Comparison of the PiezoSystems Jena actuator static linear model prediction with experimental data.

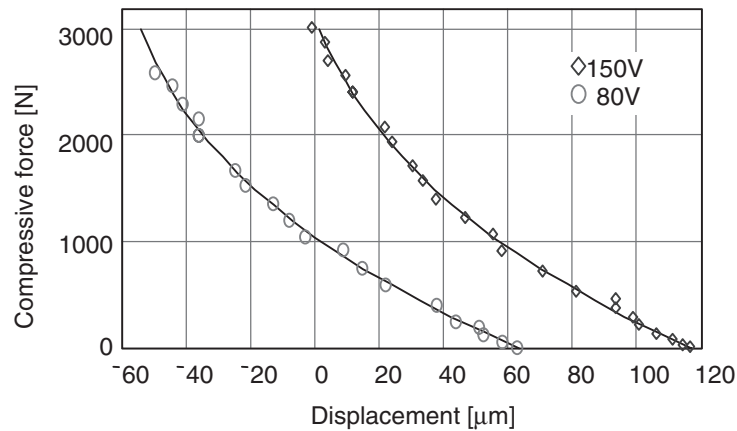


Figure 8. Curve-fitting of experimental data using a bivariate regression.

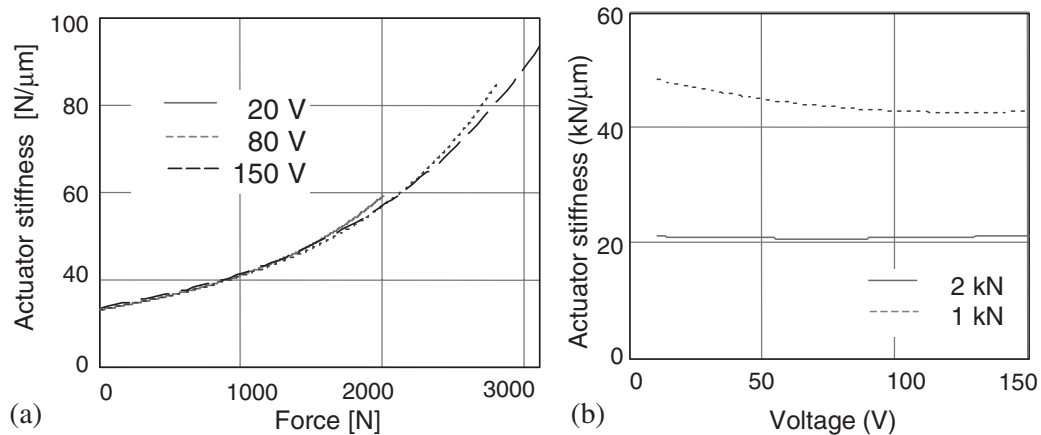


Figure 9. Actuator stiffness: (a) variation with external force; (b) variation with voltage.

behavior in terms of the force in the active material,  $F_{ST}$ , voltage,  $V$ , and actuator displacement,  $u$ , i.e.  $u = u(F_{ST}, V)$ .

The *actuator static stiffness* was determined as the local derivative of the force–displacement curve (tangent stiffness), using the inverse of the tangent compliance, i.e.  $k = (\partial u / \partial F_c)^{-1}$ . It was found (Figure 9) that the tangent stiffness of the piezoelectric actuator increased significantly with the compressive mechanical load, but varies negligibly with voltage.

The compliance and the piezoelectric coefficients were calculated by assuming  $S_{33} = s_{33}(V, F)(F + d_{33}(V, F) \cdot V$ , and taking the displacement derivatives with respect to force and voltage:

$$\begin{aligned} \frac{A}{L_i^0} \left( \frac{\partial u}{\partial F_{ST}} \right) &= s_{33} + F \frac{\partial s_{33}}{\partial F_{ST}} + \frac{A}{t} V \frac{\partial d_{33}}{\partial F_{ST}}, \\ \frac{t}{L_i^0} \left( \frac{\partial u}{\partial V} \right) &= \frac{t}{A} F_{ST} \frac{\partial s_{33}}{\partial V} + V \frac{\partial d_{33}}{\partial V} + d_{33} \end{aligned} \quad (21)$$



Neglecting the cross-coupling terms (ANSI/IEEE Std.176, 1987; Mitrovic et al., 1999) we obtain a

first-order approximation of the compliance and piezoelectric coefficients:

$$s_{33} \approx \frac{A}{L_i^0} \left( \frac{\partial u}{\partial F_{ST}} \right); \quad d_{33} \approx \frac{t}{L_i^0} \left( \frac{\partial u}{\partial V} \right) \quad (22)$$

We found that for static excitation, the compliance,  $s_{33}$ , decreases with increasing stress (Figure 10(a)) but varies very little with the electric field. The piezoelectric coefficient,  $d_{33}$  (Figure 10(b)) has a maximum value at approximately half the maximum electric field, and varies moderately with stress.

### Low-frequency Dynamic Results

The data processing flowchart is shown in Figure 11. For each frequency/prestress/voltage case, four waveforms (displacement in Figure 12(a), force in Figure 12(b), current in Figure 12(c), and voltage) were recorded and further processed in several stages using Matlab™ software. The first stage of data processing consisted in applying the calibration factors, and filtering the signal spikes using cascade algorithms for

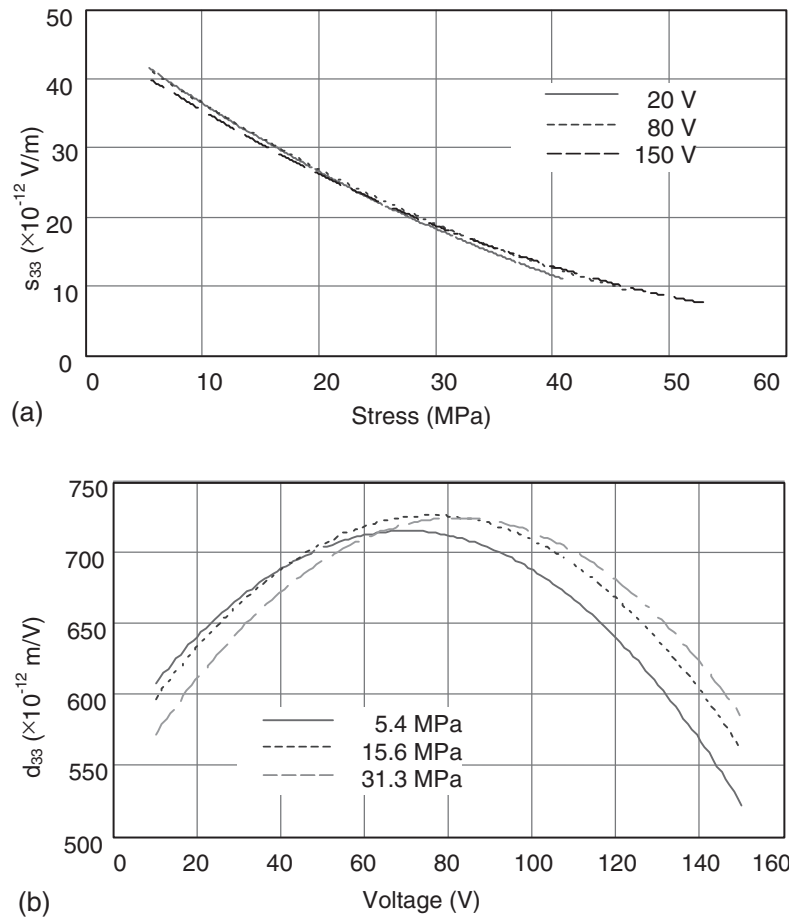


**Figure 10.** Effective piezoelectric material coefficients evaluated from the derivatives of the displacement with respect to force and voltage: (a) compliance,  $s_{33}$ ; (b) piezoelectric coefficient,  $d_{33}$ .

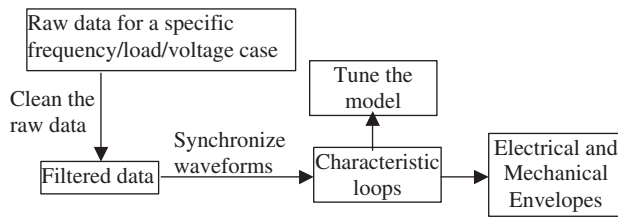


**Figure 11.** Data processing logic flow.

outlier elimination and digital Butterworth filtering. The second stage of data processing consisted of building the characteristics loops of synchronized waveforms, paired as displacement *versus* force (Figure 12(d)), current *versus* voltage (Figure 12(e)), and displacement *versus* voltage (Figure 12(f)).

The dynamic model parameters and their observed correlation with the actuator behavior are listed in Table 2. The values of these parameters were determined by tuning the theoretical model prediction to the experimental data. During this process, special attention was given to the parameters  $\varepsilon_{33}$  and  $\delta$ , which were allowed to vary during the cycle, because the

experimental data revealed significant deviations of the electric current waveforms from a harmonic form on the unloading path (Figures 12(c) and 12(e)). Since the deviations implied a reduction of the peak current and a departure from the theoretically predicted harmonic shape on the unloading path, the following nonlinear laws of  $\varepsilon_{33}$  and  $\delta$  variation inside the cycle were suggested:

$$\varepsilon_{33} = \varepsilon_0[1 - 0.5(k_\varepsilon - 1)f_e(t)(H(t_{\text{end}}) - H(t_{\text{start}}))] \quad (23a)$$

$$\delta = \delta_0[1 + 0.5(k_\delta - 1)f_e(t)(H(t_{\text{end}}) - H(t_{\text{start}}))] \quad (23b)$$

The function  $0.5f_e(t)(H(t_{\text{end}}) - H(t_{\text{start}}))$  is a smoothing window that ensures a smooth transition between the loading and unloading portions of the cycle. The parameter  $k_\varepsilon$  accounts for the reduction of the peak amplitude, while  $k_\delta$  accounts for the distortion of the harmonic shape of the electric current waveform on the unloading path. This improvement allows a more accurate tuning of the model to the experimental data. Thus, for each combination of frequency, voltage, and prestress, a set of eight effective parameters was

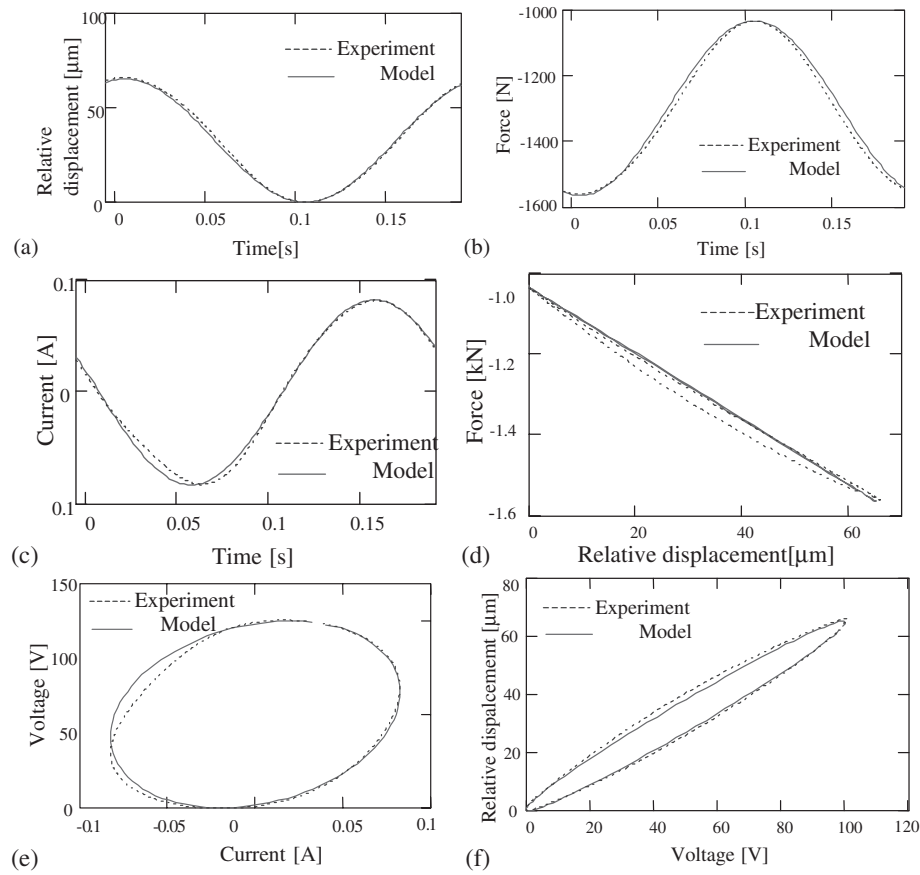


**Figure 12.** Comparison of experimental data with the model prediction for 5Hz, 1150 prestress and 0–100V: (a) displacement waveform; (b) force waveform; (c) electric current waveform; (d) displacement–force loop; (e) electric current–voltage loop; (f) voltage–displacement loop.

**Table 2. Correlation between tuning coefficients and experimental curves.**

Material Parameter	Influence on the Characteristic Curves
$d_{33}$	Proportional to the amplitude of the displacement waveform and the secant slope of the force–displacement characteristic loop;
$s_{33}$	Influences amplitudes of the force and displacement waveforms; the ratio of the stack stiffness $k_{ST}$ to the external dynamic stiffness $k_d$ influences the slope of the force–displacement loop
$\epsilon_{33}$	Related to the electric current amplitude on the loading path;
$\lambda$	Proportional with the hysteresis in the displacement–voltage characteristic loop
$\eta$	No significant influence;
$\delta$	Global tilt of the current–voltage characteristic loop.

determined:  $d_{33}$ ,  $\lambda$ ,  $s_{33}$ ,  $\eta$ ,  $\epsilon_0$ ,  $\delta_0$ ,  $k_\delta$ ,  $k_\epsilon$  (Pomirleanu, 2001). An illustration of the tuning process results is shown in Figure 13.

The third stage consisted of synthesizing the mechanical and electrical envelopes using the extreme values of

the characteristic loops (Figures 14–16). These envelopes give a general view of actuator capabilities and point to its usefulness for specific applications.

## MODELING OF MAGNETOSTRICTIVE ACTUATOR IMPEDANCE

A magnetoactive solid-state actuator consists of a Terfenol bar inside an electric coil and enclosed into an annular magnetic armature (Figure 17(a)). The ETREMA AA-140J025 actuator (Figure 17(b)) has prestress disc springs (Belleville washers) that apply a mechanical bias of 890 N, which helps orient the magnetic domains normal to the compression axis, maximizing the material magnetostriction. Since the bi-polar excitation of magnetostrictive material at low fields is nonlinear, the active material in actuator applications is subjected to a bias magnetic field,  $H_0$ , of value close to the inflection point on the strain–field curve (de Lechaisserie, 1993). Permanent magnets made of Alnico V are used to create a bias magnetic field of about 2.9 kA/m, thus bringing the zero-point operation within the middle of the quasi-linear strain–magnetic

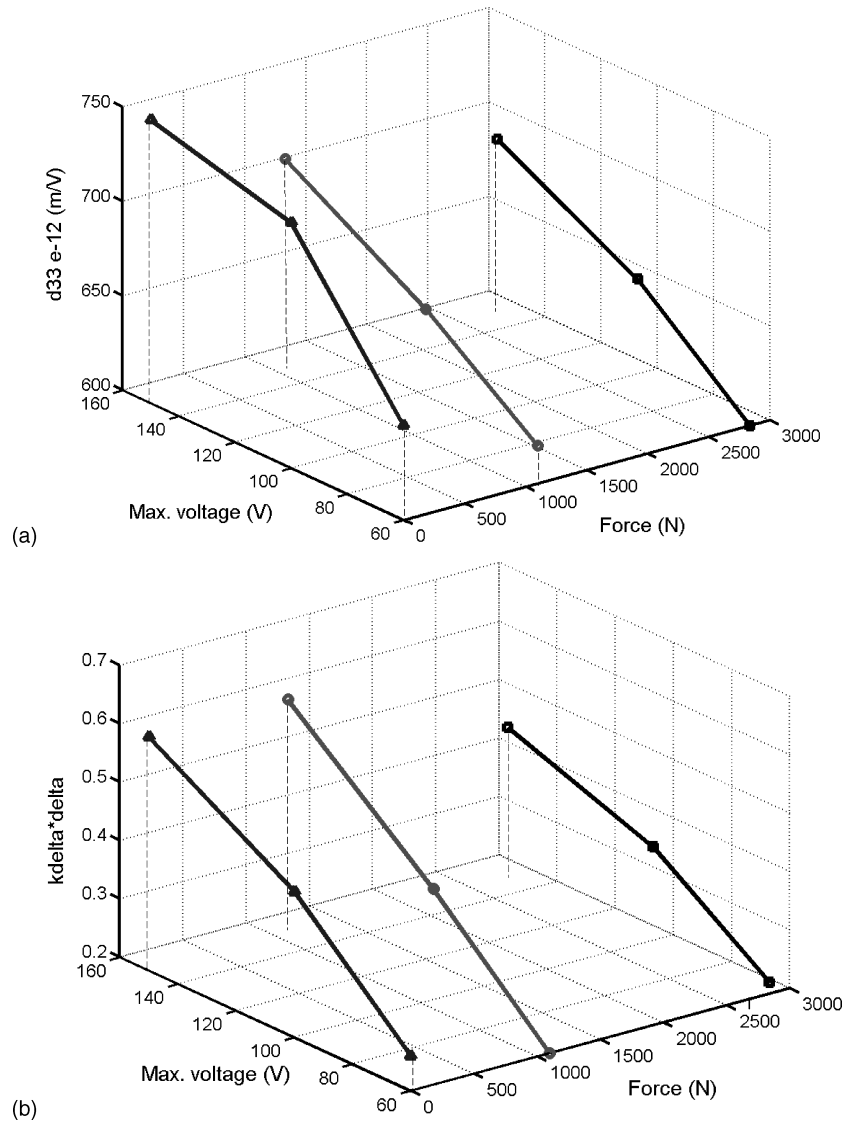


**Figure 13.** Tuned model coefficients variation with voltage and external preload force, at 1 Hz: (a) piezoelectric coefficient,  $d_{33}$ ; (b) peak losses on the unloading path,  $k_{\delta} \cdot \delta$ .

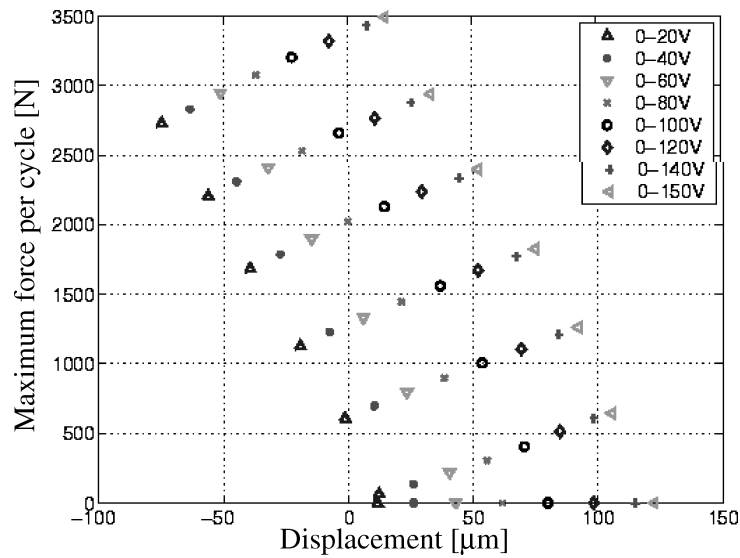


**Figure 14.** Mechanical envelope for the piezoelectric actuator PiezoSystems Jena PAHL 120/20 under dynamic testing at 5 Hz.

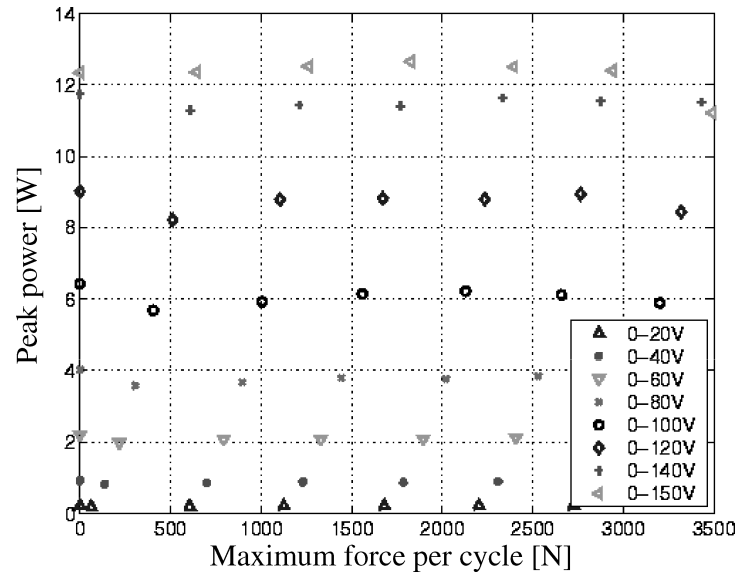


Figure 15. Electrical envelope for the PiezoSystems Jena PAHL 120/20: peak power at 5 Hz.

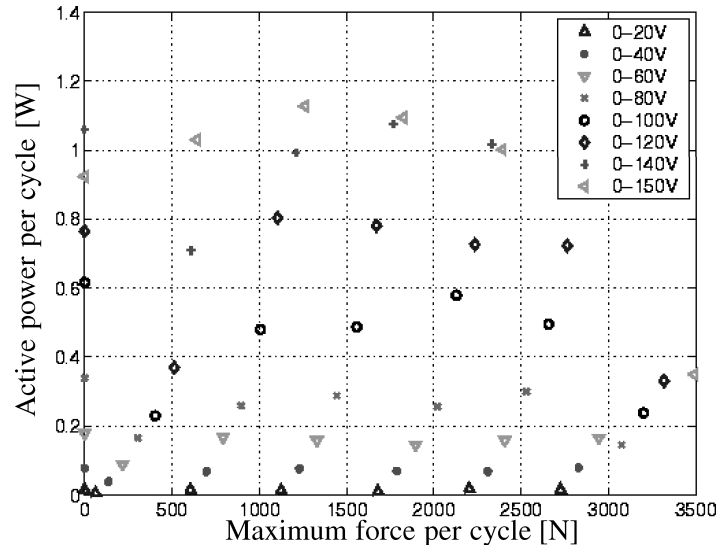


Figure 16. Electrical envelope for the PiezoSystems Jena PAHL 120/20: active power at 5 Hz.

field characteristic. The Alnico V permanent magnet is slit longitudinally to minimize eddy currents losses. The magnetostrictive material behaves quasi-linearly about the bias point, as described by the piezomagnetic constitutive equations:

$$S_{ij} = s_{ijkl}^{(H)} T_{kl} + d_{ijm} H_m \quad B_i = d_{ijk} T_{jk} + \mu_{im}^{(T)} H_m \quad (24)$$

where, in addition to the already defined variables,  $H_m$  is the magnetic field vector,  $B_m$  is the magnetic induction vector,  $d_{ijk}$  is the piezomagnetic coupling tensor, and  $\mu_{im}^{(T)}$  is the magnetic permeability tensor at constant stress.

The coefficients of Equations (24) vary strongly with amplitude, since they only represent a local linearization of inherently nonlinear equations. Different material

coefficients (compliance, piezomagnetic, and permeability) have to be used for each point of operation.

Electric power requirements are a major factor in designing active-material actuation systems. To determine the power consumption, one has to know the actuator impedance and its variation with electric current, voltage, and frequency. Vendor data usually provides impedance frequency spectrum at very small voltage values. However, several studies have shown that the impedance spectrum strongly depends on the driving field intensity and on the stress levels (Dapino et al., 1998). Magnetostrictive actuators impedance modeling must account for both the active material behavior and the physics of magnetization outside the Terfenol-D rod. Let all the quantities in the constitutive Equations (24) have a harmonic variation around a bias value, i.e.  $a(r, \tau) = A_0 + A(r)e^{i\omega\tau}$ , where  $A_0$  is the bias

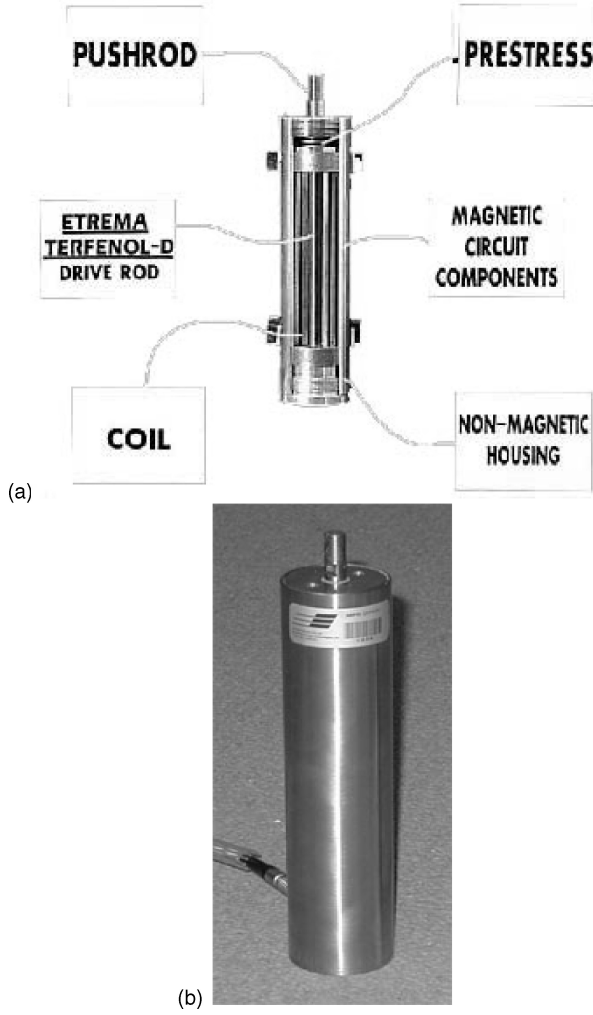


**Figure 17.** (a) Cross-section through an induced-strain actuator using a TERFENOL magnetoactive rod (ETREMA Products, Inc.); (b) AA140J025 magnetostrictive actuator.

value and  $A$  is the alternating part. The bias stress,  $T_0$ , bias strain  $S_0$ , bias magnetic field  $H_0$ , and bias magnetic induction  $B_0$  satisfy the constitutive equations in the absence of forcing loads (externally applied stress or magnetic field), and consequently so do the alternating parts of stress, strain, magnetic field, and induction. Assuming further that only axial effects along the Terfenol-D rod are important, the constitutive equations simplify to:

$$S_3 = s_{33}^{(H)} T_3 + d_{33} H_3 \quad B_3 = d_{33} T_3 + \mu_{33}^{(T)} H_3 \quad (25)$$

where  $d_{33}$  is the piezomagnetic coefficient relating applied magnetic field to induced strain,  $H_3$  is the applied magnetic field,  $B_3$  is the magnetic flux density, and  $\mu_{33}^{(T)}$  is the magnetic permeability. Similarly with the piezoelectric material case, magnetic and mechanical losses inside the magnetostrictive material can be

modeled using the complex compliance,  $s_{33}^{(H)*} = s_{33}^{(H)*} (-i\delta)$  and the complex magnetic permeability,  $\mu_{33}^{(T)*} = \mu_{33}^{(T)*} (1 - i\delta)$ .

The motion equation,  $\rho \ddot{u} = \nabla \cdot \mathbf{T}$ , simplified for small strains and under the assumption of axial effects only takes the form of Equation (3), where the stress gradient in the  $x_3$  direction is determined similarly with the piezoelectric case,

$$\begin{aligned} \frac{\partial T_3}{\partial x_3} &= \frac{\partial}{\partial x_3} \left( \frac{1}{s_{33}^{(H)}} S_3 - \frac{d_{33}}{s_{33}^{(H)}} H_3 \right) \\ &= \frac{\partial}{\partial x_3} \left( \frac{1}{s_{33}^{(H)}} S_3 - \frac{d_{33}}{s_{33}^{(H)}} \left( \frac{1}{\mu_{33}^{(T)}} B_3 - \frac{d_{33}}{\mu_{33}^{(T)}} T_3 \right) \right) \quad (26) \\ &= \frac{1}{s_{33}^{(H)}} \frac{\partial S_3}{\partial x_3} + \frac{d_{33}^2}{s_{33}^{(H)} \mu_{33}^{(T)}} \frac{\partial T_3}{\partial x_3} - \frac{d_{33}}{s_{33}^{(H)} \mu_{33}^{(T)}} \frac{\partial B_3}{\partial x_3} \end{aligned}$$

and since  $\nabla \cdot \mathbf{B} \cong \partial B / \partial x_3 = 0$ , we further have:

$$\begin{aligned} \frac{\partial T_3}{\partial x_3} &= \frac{1}{s_{33}^{(E)} \left( 1 - (d_{33}^2 / (s_{33}^{(E)} \mu_{33}^{(T)})) \right)} \frac{\partial S_3}{\partial x_3} \\ &= \frac{1}{s_{33}^{(E)} (1 - \kappa_{33}^2)} \frac{\partial^2 u_3}{\partial x_3^2} = \frac{1}{s_{33}^{(D)}} \frac{\partial^2 u_3}{\partial x_3^2} \quad (27) \end{aligned}$$

The motion equation is thus written as:

$$\frac{\partial^2 u_3}{\partial \tau^2} = \frac{1}{c^{*2}} \frac{\partial^2 u_3}{\partial x_3^2} \quad (28)$$

where  $c^{*2} = 1 / \rho s_{33}^{(B)*}$  is the complex wave speed.

The boundary conditions for the alternating part of the mechanic variables are:

$$u_3(x = 0, \tau) = 0 \quad (29)$$

$$A_T \cdot T_3(L_T, \tau) = F_{\text{EXT}}(\tau) = -k_{dm}(\omega) \cdot u_3(L_T, \tau) \quad (30)$$

where  $F_{\text{EXT}}$  is the force exerted by the magnetostrictive rod on the external load, and  $k_{dm}$  is the dynamic stiffness of the external structure. The excitation current is sinusoidal:  $I(\tau) = I e^{i\omega\tau}$ . For the present study, only the internal prestress spring and the push rod interact dynamically with the Terfenol-D rod, and thus the external dynamic stiffness is:

$$k_{dm}(\omega) = m(\omega_n^2 - \omega^2 + 2i\zeta \omega \omega_n) \quad (31)$$

where  $\omega_n = (k_{SP}/m_{\text{rod}})^{0.5}$  is the natural frequency, and  $m_{\text{rod}}$  is the push rod mass. The stiffness of the internal spring was assumed constant.

Denote  $\gamma = \omega/c^*$ , and consider only the harmonic part of the actuator displacement:  $u(x_3, \tau) = (C_1 \sin(\gamma x_3) + C_2 \cos(\gamma x_3)) e^{i\omega\tau}$ . Applying the first boundary condition

(Equation (29)) yields  $C_2 = 0$ , while the second boundary condition (Equation (30)) furnishes  $C_1$ :

$$C_1 = d_{33} H_3 \left[ \left( 1 + \frac{k_{dm}(\omega) \tan(\gamma L_T)}{k_T} \right) \gamma \cos(\gamma L_T) \right]^{-1} \quad (32)$$

where  $k_T$  is the complex stiffness of the magnetostrictive rod,

$$k_T = \frac{A_T}{s_{33}^{*(H)} L_T} \quad (33)$$

with  $A_T$  and  $L_T$  being the area and length of the TERFENOL-D material respectively.

Using the second constitutive equation, the amplitude of the induction is:

$$\begin{aligned} B_3(x_3) &= \frac{d_{33}}{s_{33}^{*(H)}} \left( \frac{\partial u_3}{\partial x_3} - d_{33} H_3 \right) + \mu_{33}^{*(T)} H_3 \\ &= \frac{d_{33}^2}{s_{33}^{*(H)}} H_3 \left( \left( 1 + \frac{k_{dm}(\omega) \tan(\gamma L_T)}{k_T} \right)^{-1} \frac{\cos(\gamma x_3)}{\cos(\gamma L_T)} \right. \\ &\quad \left. - 1 + \frac{\mu_{33}^{*(T)} s_{33}^{*(H)}}{d_{33}^2} \right) \end{aligned} \quad (34)$$

The back emf in the coil along the Terfenol-D rod due to variable flux is:

$$\begin{aligned} e(x_3) &= -N \frac{d}{dt} \int_{A_T} \hat{B}_3 dA \\ &= -i\omega N \frac{d_{33}^2}{s_{33}^{*(H)}} \left( \left( 1 + \frac{k_{dm}(\omega) \tan(\gamma L_T)}{k_T} \right)^{-1} \frac{\cos(\gamma x_3)}{\cos(\gamma L_T)} \right. \\ &\quad \left. - 1 + \frac{\mu_{33}^{*(T)} s_{33}^{*(H)}}{d_{33}^2} \right) \int_{A_T} H_3 dA \end{aligned} \quad (35)$$

where  $N$  is the number of coil turns and an ideal return path for the magnetic circuit was assumed. The non-uniform radial distribution of the magnetic field gives rise to eddy currents in the Terfenol-D rod (Hall and Flatau, 1995; Engdahl, 2000). While these effects are expected to be small in the permanent magnet because of its slit geometry, the eddy currents in the magnetostrictive rod generate ohmic losses that can be taken into account through a complex frequency-dependent coefficient,  $\chi = \chi_i - i \cdot \chi_r$ , where

$$\begin{aligned} \chi_r &= \frac{2}{k_z r_T} \frac{\text{ber}(k_z r_T) \cdot \text{bei}'(k_z r_T) - \text{bei}(k_z r) \cdot \text{ber}'(k_z r_T)}{\text{ber}(k_z r_T)^2 + \text{bei}(k_z r_T)^2} \\ \chi_i &= \frac{2}{k_z r_T} \frac{\text{ber}(k_z r_T) \cdot \text{ber}'(k_z r_T) - \text{bei}(k_z r) \cdot \text{bei}'(k_z r_T)}{\text{ber}(k_z r_T)^2 + \text{bei}(k_z r_T)^2} \end{aligned} \quad (36)$$

where  $k_z = \sqrt{\omega \mu_{33}^{*(S)} \sigma}$ ,  $r_T$  is the Terfenol-D rod radius,  $\sigma$  is the Terfenol-D conductivity, and “ber” and “bei” are the Kelvin functions defined by:  $J_0(i\sqrt{ix}) = \text{ber}(x) + i \cdot \text{bei}(x)$  (Engdahl, 2000). This coefficient relates the effective magnetic flux density to the external magnetizing field. In terms of modeling, the complex coefficient  $\chi$  multiplies the real part of the Terfenol-D rod static magnetic permeability, and thus the effective magnetic permeability becomes

$$\mu_{33\text{Lys}}^{*(T)} = (\chi_r - i\chi_i) \mu_{33}^{*(T)} - \delta \mu_{33}^{*(T)} = \mu_{33}^{*(T)} (\chi_r - i(\delta + \chi_i)) \quad (37)$$

The back emf amplitude across the actuator leads follows from integrating Equation (35):

$$e = -i\omega A_T \frac{N^2}{L} I \frac{d_{33}^2}{s_{33}^{*(H)}} \left( \left( 1 + \frac{k_{dm}(\omega) \tan(\gamma L_T)}{k_T} \right)^{-1} \frac{\tan(\gamma L_T)}{\gamma L_T} - 1 + \frac{\mu_{33\text{Lys}}^{*(T)} s_{33}^{*(H)}}{d_{33}^2} \right) \quad (38)$$

For an ideal return path for the magnetic circuit, the leakage resistance due to nonuniform variation of the magnetic field along the  $x_3$  direction can be neglected. The leakage inductance due to the gap between coil and magnetostrictive core can be written as (Engdahl, 2000):

$$\begin{aligned} L_{\text{coil\_leakage}} &= G_{\text{coil}}^2 N^2 \pi^2 \mu_0 \left( r_T \frac{(\lambda^2 - 1)(\alpha + 1)}{\lambda(\alpha - 1)} \right. \\ &\quad \left. + \frac{1}{6} r_{\text{coil\_I}} (\alpha + 1)(\alpha + 3) \right) \end{aligned} \quad (39)$$

where  $\alpha$  is the ratio of outer and inner coil radii,  $\beta$  is the ratio of the coil length to its diameter,  $\lambda$  is the ratio of coil inside diameter to magnetostrictive rod diameter, and  $G_{\text{coil}}$  is the coil Fabry factor, defined by:

$$G_{\text{coil}} = 0.2 \sqrt{\frac{2\pi\beta}{\alpha^2 - 1}} \ln \frac{\alpha + \sqrt{\alpha^2 + \beta^2}}{1 + \sqrt{1 + \beta^2}} \quad (40)$$

The Kirchhoff law written for the circuit in Figure 18(a) that models the experiment circuit is  $V = I \cdot (R_{\text{DC}} + Z_{\text{CO}} + Z_{\text{leakage}}) - e$ , where  $U_T = I \cdot (Z_{\text{leakage}} + R_{\text{DC}}) - e$  is the voltage drop across the actuator,  $R_{\text{DC}}$  is the DC coil resistance,  $Z_{\text{leakage}}$  corresponds to  $L_{\text{coil\_losses}}$ , and  $Z_{\text{CO}}$  is the impedance of a mainly resistive circuit element used to monitor current levels. Within the bounds



of linear magnetostrictive theory, the actuator impedance is:

$$Z_T = \frac{U_T}{I} = -\frac{e}{I} + i\omega L_{\text{coil\_leakage}} + R_{\text{DC}}$$

$$= i\omega \left[ \frac{N^2 A_T d_{33}^2}{L_T s_{33}^{*(H)}} \left( \left( 1 + \frac{k_{dm}(\omega) \tan(\gamma L_T)}{k_T \gamma L_T} \right)^{-1} \frac{\tan(\gamma L_T)}{\gamma L_T} - 1 + \frac{\mu_{33}^{*(T)} s_{33}^{*(H)}}{d_{33}^2} \right) + L_{\text{coil\_leakage}} \right] + R_{\text{DC}}$$
(41)

### TESTING OF THE MAGNETOSTRICTIVE ACTUATOR



The experiments performed on the Etrema AA-140J025 magnetostrictive actuator were done in two stages. In the first stage, the low-power impedance (1 V<sub>pp</sub> excitation) was determined using an HP 4194A Impedance Analyzer (Figure 18(a)). This measurement was performed over the 100–3500 Hz frequency range, with the resonance observed around 3 kHz. The measured real and imaginary parts of the impedance were downloaded in a PC. In the second stage, the full-power impedance was measured in the range 1–2 kHz, using an experimental setup consisting of a HP3312A function generator, a Compact Power MAC-01 amplifier, a Tektronix TDS 210 oscilloscope, and a calibrated resistor for on-line electric current monitoring (Figure 18(b)). The calibrated resistor was placed in series with the actuators. The resistor was built from constantan wire, which has low dependence of resistivity with temperature. DC and AC measurements of the calibrated resistor were performed with electric currents up to 0.5 A, and at frequencies up to 5 kHz. The calibrated resistor showed a resistance of 0.92 Ω and an inductance of 3.67 μH.

During the stage two experiments, the harmonic voltage signals across the calibrated resistor and across

the entire series circuit were simultaneously displayed on the Tektronix TDS 210 oscilloscope, allowing for the measurement of the voltage, electric current determined from the voltage drop across the calibrated resistor, and the relative phase lag induced by the magnetostrictive actuator. The full-power measurements could only be taken at frequencies above 1 kHz, due to the combination of minimum output voltage of the voltage amplifier and electric current limitations of the actuator. The testing procedure consisted of:

- Set an input voltage  $U_k$ , such that the current at 1 kHz would not exceed 3A RMS;
- Sweep the frequency between 1 and 2 kHz in steps of 100 Hz and record the voltage across the entire circuit  $U$ , the voltage across the calibrated resistor  $U_{CO}$ , and the phase lag between these two signals
- Calculate a new maximum input voltage  $U_{k+1}$  using the impedance calculated with the data recorded in step (b). Then, repeat steps (a) and (b), until  $U_{k+1}$  would induce a current greater than 3A RMS, at 1 kHz.

### DATA PROCESSING AND MODEL TUNING FOR THE MAGNETOSTRICTIVE ACTUATOR

To determine the electrical impedance from the experimental data, the Etrema magnetostrictive actuator was electrically modeled as a series RL circuit (Hall and Flatau, 1995; Engdahl, 2000). The entire electrical circuit could be simply represented in the phasors space as shown in Figure 19(b). The measured electrical impedance of the actuator can be written as:

$$Z_T = \frac{U_T}{I} = \frac{\sqrt{U^2 + U_{CO}^2 - 2U_{CO}U \cos(\varphi)}}{U_{CO}/R_{CO}} \quad (42)$$

where the inductance of the constantan resistor was assumed too small to significantly influence the phase

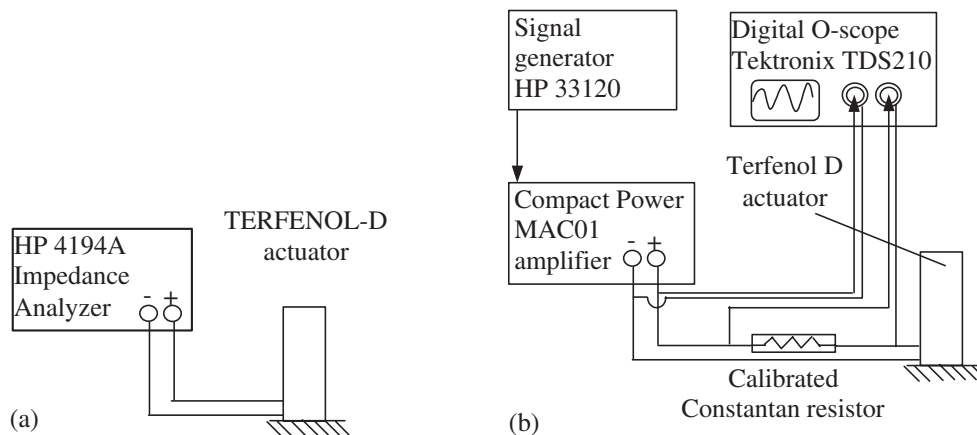


Figure 18. Experimental setup for determining the actuator electrical impedance: (a) low-power experiments; (b) full-power experiments.

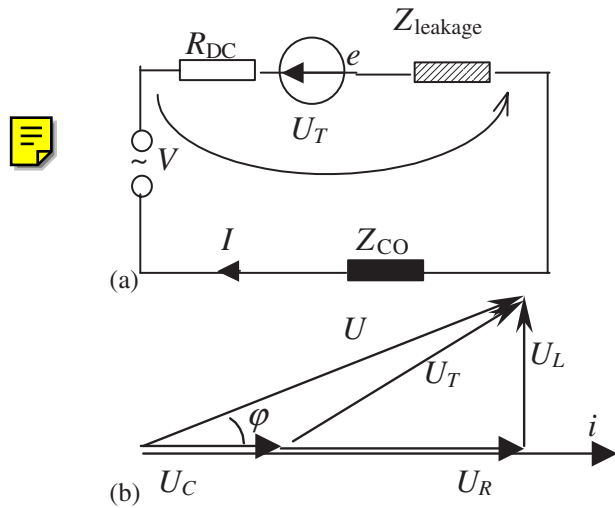


Figure 19. (a) Testing electric circuit; (b) Phasors diagram for the Etrema actuator measurement circuit.

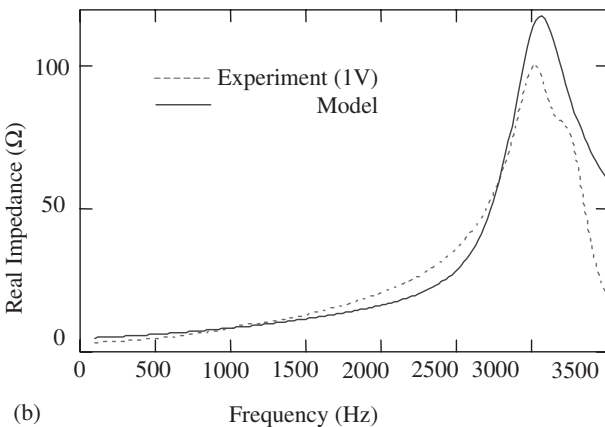
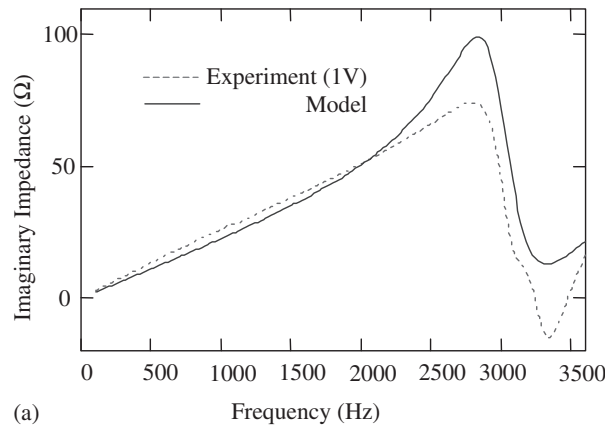


Figure 20. Etrema AA140J250 impedance for 1V excitation voltage: (a) imaginary impedance; (b) real impedance.

lag between electric current and voltage across the actuator, approximated by the measured phase lag between  $U$  and  $U_{CO}$ .

The model was first tuned on the impedance analyzer experimental data using the model parameters  $s_{33}^{(H)}$ ,

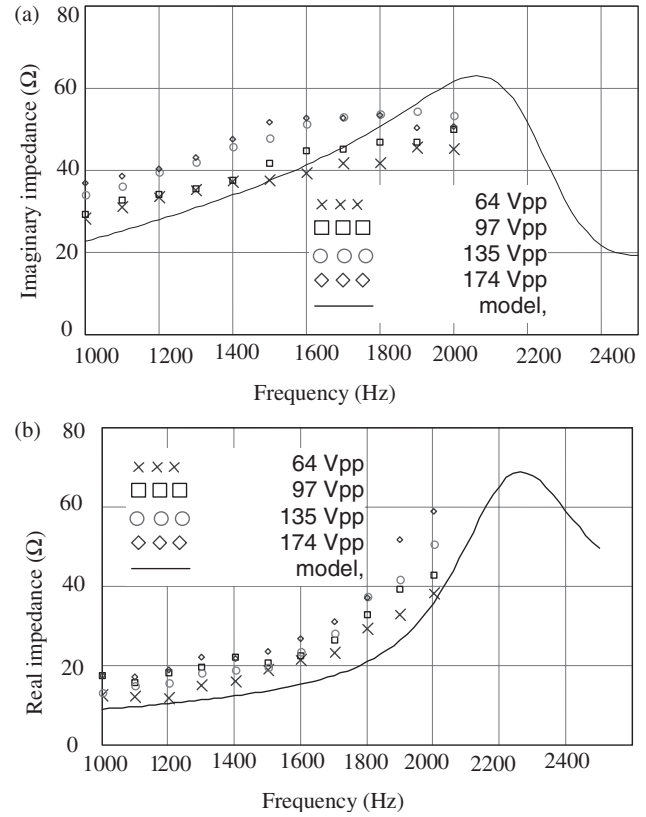


Figure 21. Actuator impedance under high driving fields: (a) imaginary impedance; (b) real impedance.

$\mu_3^{(T)}$ ,  $d_{33}$ ,  $\eta$ , and  $\delta$ . The low-voltage data was chosen because the actuator nonlinearities are weaker at low-excitation fields. Figure 20 compares the theoretical and experimental real and imaginary impedance. The actuator behavior under high driving field shows a shift in the antiresonant frequency (Dapino et al., 1998), due to the Young's modulus decrease (Faidley et al., 1998), and possibly due to nonlinearities associated with the internal prestress spring. The linear model is able to capture this trend through magnetostrictive material parameters retuning (Figure 21).

## DISCUSSION

### Piezoelectric Actuator Characterization

The static blocked force was measured using two different methods. The results obtained with these methods differed from each at high-field levels. At maximum voltage, a significant difference between the two measurements methods was observed. These results indicate that at low and moderate electric fields the hypothesis of linear superposition holds for the tested piezoelectric actuator. At high electric fields, ferroelastic and ferroelectric switching time-history effects become

important, since the same inputs applied in a different order lead to different electro-mechanical equilibrium states. The explanation for this behavior may reside in the different ferroelastic domain switching that occurs when the order of loading is changed. At small electric fields and stress, the domain switching is insignificant and the piezoelectric material behavior is linear. At moderate fields, the material domain switching under stress loading starts occurring, but the stress levels are not high enough to prevent the domain switching reversal upon the application of electric field needed to simulate blocked force conditions. At large stresses, some 90°-switched domains are no longer able to revert the switching upon electric field application, if the second method of blocked force testing is used. However, with the prior application of the electric field as with the first method, some of the domains will no longer switch under the application of the stress needed to simulate the blocked force condition. The amount of domain switching depends on the piezoelectric material formulation and on the particular design of the actuator.

For dynamic loading, an almost linear correlation of the blocked force with applied voltage was observed. This may be attributed to the ferroelectric/elastic switching effects reaching a state of dynamic equilibrium, minimizing the time-history effects of the loading. For dynamic applications, effective values of model parameters (Pomirleanu, 2001) were obtained for the tested actuator in a cycle-averaged sense. The tuned data suggests that the cycle-equivalent value of the  $d_{33}$  coefficient increases with voltage, consistent with the corresponding static data (Figure 10(b)), if the bias voltage is substituted for the static voltage.

The electrical envelopes for the maximum peak power show a consistent dependence on frequency, force, and voltage cycle, qualifying the peak power as a useful evaluator of a piezoelectric actuator for a specific application. The peak power was found to be proportional to the applied voltage and frequency, and also to increase with force (Figure 15). This increase may be due to an increased dielectric permittivity along a direction that is no longer aligned with the dipole axis of the PZT crystal, due to inherent crystal anisotropy (Du et al., 1997; Uchino, 2000). At higher stresses, more ferroelastic switching occurs, leading to more domains having their electric dipoles misaligned from the  $x_3$  axis, which results in an increased permittivity at the polycrystallite level. This explanation also correlates with the behavior of the cycle-equivalent electrical permittivity,  $\epsilon_{33}$  (Pomirleanu, 2001).

The average active power per cycle (Figure 16) appears to increase with voltage and decrease with prestress level. The increase with voltage is more pronounced than predicted by the theory for a constant dielectric loss coefficient,  $\delta$ . The difference may be

explained through domain switching as follows: at a given voltage cycle, the prestress increase will impede more domains from ferroelastic switching, while at a given prestress level, the voltage increase will help more domains to perform 90° switching. Since ferroelastic switching is associated with energy loss (Kessler and Balke, 2001; Chaplya and Carman, 2002), the increase of active power consumption is immediate. These observations correlate with the model coefficients mostly through the variation of the  $\delta_0 \cdot k_\delta$  product (Table 3), that represents the peak dielectric loss on the unloading cycle. This quantity represents a better modeling parameter than  $k_\delta$ , since it captures both the above-mentioned measured trends seen in the active power envelopes, and its variation is contained within a narrower range (Pomirleanu, 2001).

### Magnetostrictive Actuator Characterization

Previous studies (Goodfriend, 1992) as well as manufacturer data, placed the compliance coefficient between  $28 \times 10^{-12}$  and  $47 \times 10^{-12} \text{ m}^2/\text{N}$ , the relative magnetic permeability  $\kappa_M = \mu_M/\mu_0$  between 3 and 10, and the piezomagnetic coefficient between 8 and 20 nm/A. The cycle-averaged values used by the linear magnetostrictive follow these guidelines closely (Table 4). Although the magnetostrictive material is expected to behave linearly for small driving fields, and the tuned model to follow closely the experimental curves, the mismatch in the resonance region is probably due to the nonlinear effects occurring at resonance.

**Table 3. Etrema AA-140J025 magnetostrictive actuator properties.**

Current range	0–3 ARMS
Temperature range	–20 to 100°C
Maximum dynamic force	± 890 N
Maximum blocked force	1740 N
DC resistance	2.3 Ω
Inductance (up to resonance)	3.5 mH
Natural frequency	2.4 kHz
Length	198 mm
Diameter	47 mm
Number of turns in the coil	1070
Length of the Terfenol-D rod	152.4 mm
Area of the Terfenol-D rod	126.45 mm <sup>2</sup>
Density of Terfenol-D	9183 kg/m <sup>3</sup>

**Table 4. Relative magnetic permeability tuning using the experimental impedance value for the magnetostrictive actuator.**

Voltage Across Actuator (VRMS)	$\kappa_M = \mu_{33}/\mu_0$	$S_{33}^{(H)} \times 10^{-11} \text{ N m}^{-2}$	$\eta$	$\delta$	$\zeta$
≈ 1	2.5	2.7	0.05	0.05	0.1
45.3	4.5	5.2	0.1	0.15	0.1

Model tuning using experimental data was based exclusively on the magnetic permeability and compliance coefficients, since the actuator displacement was not measured. The shift of the resonance peaks at high driving fields can be explained through the magnetostrictive material Young's modulus dependence on the magnetic driving field (Dapino et al., 1998), and the internal spring stiffness variation with load, since this actuator uses nonlinear Belleville washer springs.

## CONCLUSIONS

The loads superposition principle was found valid only up to 70% of the maximum voltage for the tested piezoelectric actuator under high electro-mechanical static loading. A significant nonlinearity in the static mechanical envelope was also observed. However, for dynamic loading, this nonlinearity is much less pronounced. A quasi-linear model was employed for dynamic analysis. Cycle-averaged parameters were evaluated. Model tuning was performed to fit the experimental data and the linear model was improved to include higher dielectric losses on the unloading path. We found that the peak dielectric loss on the unloading path increased with the AC voltage amplitude and decrease with the prestress level. The measurements of the peak and active power consumed by the piezoelectric actuator showed consistent dependence of these quantities on prestress level and voltage duty-cycle.

The magnetostrictive actuator electrical impedance was modeled using a quasi-linear model. Experiments at low and high power allowed tuning of the quasi-linear model. The model can accommodate the left shift of the antiresonance/resonance frequency through Young's modulus decrease and magnetic permeability increase. However, due to the inherent higher nonlinearity of the magnetostrictive material and the fact that the corresponding model was applied to a wider frequency range, the tuned piezoelectric actuator model is a better predictor than the magnetostrictive actuator model.

## NOMENCLATURE

$A$  = cross-sectional area of the stack  
 $L$  = length of the stack  
 $t$  = active layer thickness  
 $S_3$  = contracted notation for the strain in the polarization direction,  $S_{33}$   
 $T_3$  = contracted notation for the stress  $T_{33}$

$D_3$  = electric displacement in the polarization direction  
 $E_3$  = electric field in the polarization direction  
 $F_{ST}$  = force exerted in the piezoelectric stack  
 $d_{33}$  = contracted notation for the  $d_{333}$  piezoelectric or piezo-magnetic coefficient  
 $s_{33}$  = contracted notation for the  $s_{3333}$  compliance coefficient  
 $\epsilon_{33}$  = electric permittivity  
 $\mu_{33}$  = magnetic permeability  
 $k_{ST}$  = stack stiffness  
 $k_{SP}$  = internal spring stiffness  
 $c_d$  = external structure viscous damping  
 $m$  = external mass  
 $k_e$  = external stiffness  
 $F_0$  = prestress force  
 $c$  = wave speed  
 $\tau$  = time  
 $\rho$  = density  
 $\eta$  = elastic loss  
 $\delta$  = hysteretic loss (dielectric or magnetic hysteresis)  
 $\gamma$  = ratio  $\omega/c$   
 $\lambda$  = piezoelectric energy conversion loss  
 $i_{ST}$  = electric current  
 $v$  = voltage

## REFERENCES

- Ackerman, A.E., Liang, C. and Rogers, C.A. 1996. "Dynamic Transduction Characterization of Magnetostrictive Actuators," *Smart Materials and Structures*, 5(2):115–120.
- ANSI/IEEE, 1987 *IEEE Standard on Piezoelectricity*, Std. 176, IEEE, New York.
- Brennan, M.C. and McGowan, A.M. 1997. "Piezoelectric Power Requirements for Active Vibration Control," In: *Proceedings on SPIE 4th Annual Symposium on Smart Structures and Materials: Mathematics and Control with Smart Structures*, March 3–6, San Diego, CA, Vol. 3039, pp. 660–669.
- Butler, J.L. 1988. "Application Manual for the Design of Etrema™ Terfenol-D Magnetostrictive Transducers," Ames IA, Edge Technologies.
- Calkins, F.T., Smith, R.C. and Flatau, A.B. 1997. "An Energy-Based Hysteresis Model for Magnetostrictive Transducers," ICASE Report No. 97–60.
- Carman, G.P. and Mitrovic, M. 1995. "Nonlinear Constitutive Relations for Magnetostrictive Materials with Applications to 1-D Problems," *Journal of Intelligent Materials Systems and Structures*, 6(5):673–683.
- Chaplya, P.M. and Carman, G.P. 2001. "Dielectric and Piezoelectric Response of Lead Zirconate–Lead Titanate at High Electric and Mechanical Loads in Terms of non-180° Domain Wall Motion," *Journal of Applied Physics*, 90(10):5278–5286.
- Chaplya, P.M. and Carman, G.P. 2002. "Compression of Piezoelectric Ceramic at Constant Electric Field: Energy Absorption through non-180° Domain-Wall Motion," *Journal of Applied Physics*, 92(3):1504–1510.
- Chen, X., Fang, D.N. and Hwang, K.C. 1997. "Micromechanics Simulation of Ferroelectric Polarization Switching," *Acta Materialia*, 45(8):3181–3189.

- Ching-Yu Lin and Hagood, N.W. 2000. "Compression Depolarization of PZT Piezoelectric Materials under High Electromechanical Driving Levels," In: *Proceedings of SPIE Conference on Smart Structures and Materials 2000: Active Materials: Behavior and Mechanics*, Newport Beach, CA, Vol. 3992, pp. 114–125.
- Clark, A.E. 1980. "Magnetostrictive Rare Earth-Fe<sub>2</sub> Compounds," In: Wohlfarth, E.P. (ed.), *Ferromagnetic Materials*, pp. 531–589, North-Holland Publishing Co.
- Clark, A.E. 1993. "High Power Rare Magnetostrictive Materials," *Journal of Intelligent Materials Systems and Structures*, 4(1):70–75.
- Dapino, M.J., Calkins, F.T. and Flatau, A.B. 1998. "On Identification and Analysis of Fundamental Issues in Terfenol-D Transducer Modeling," In: *Proceedings SPIE Conference on Smart Structures and Materials*, San Diego, CA, Vol. 3329, pp. 185–197.
- de Lacheisserie, E.T. 1993. *Magnetostriction – Theory and Applications of Magnetoelasticity*, CRC Press.
- Du, X., Belegundu, U. and Uchino, K. 1997. "Crystal Orientation Dependence of Piezoelectric Properties in Lead Zirconate Titanate: Theoretical Expectations for Thin Films," *Japanese Journal of Applied Physics*, 37(Part 1,9A):5580–5587.
- Engdahl, G. 2000. *Handbook of Giant Magnetostrictive Materials*, Academic Press.
- Faidley, L.E., Lund, B.J., Flatau, A.B. and Calkins, F.T. 1998. "Terfenol-D Elasto-Magnetic Properties under Varied Operating Conditions using Hysteresis Loop Analysis," *SPIE Symposium on Smart Structures*, March 1998, Paper No. 3329-92.
- Faidley, L.E., Dapino, M.J. and Flatau, A.B. 2001. "Characterization of a Small Terfenol-D Transducer in Mechanically Blocked Configuration," In: *Proceedings of SPIE*, Vol. 4327, pp. 521–523.
- Fan, J., Stoll, W.A. and Lynch, C.S. 1999. "Nonlinear Constitutive Behavior of Soft and Hard PZT: Experiments and Modeling," *Acta Materialia*, 47(17):4415–4425.
- Giurgiutiu, V. and Rogers, C.A. 1996. "Power Energy Characteristics of Solid State Induced-Strain Actuators for Static and Dynamic Applications," *Journal of Intelligent Material Systems and Structures*, 7(6):656–667.
- Goodfriend, M.J. and Shoop, K.M. 1992. "Adaptive Characteristics of the Magnetostrictive Alloy, Terfenol-D, for Active Vibration Control," *Journal of Intelligent Material Systems and Structures*, 3(2):245–254.
- Hall, D.L. and Flatau, A.B. 1995. "One-Dimensional Analytical Constant Parameter Linear Electromechanical Models of a Cylindrical Magnetostrictive (Terfenol-D) Transducer," *Journal of Intelligent Materials Systems and Structures*, 6(3):315–328.
- Holland, R. 1967. "Representation of Dielectric, Elastic and Piezoelectric Losses by Complex Coefficients," *IEEE Transaction on Sonics and Ultrasonics*, SU-14(1):18–20.
- Huber, J.N. and Fleck, N.A. 2001. "Multi-Axial Electrical Switching of a Ferroelectric: Theory versus Experiment," *Journal of Mechanics and Physics of Solids*, 49(4).
- Hwang, S.C. and McMeeking, R.M. 2000. "A Finite Element Model of Ferroelectric/Ferroelastic Polycrystals," In: *Proceedings on SPIE Conference on Smart Structures and Materials 2000: Active Materials: Behavior and Mechanics*, Newport Beach, CA, Vol. 3992, pp. 404–417.
- Ikeda, T. 1990. *Fundamentals of Piezoelectricity*, Oxford Science Publications, New York.
- Jordan, T., Ounaies, Z., Tripp, J. and Tcheng, P. 2000. "Electrical Properties and Power Considerations of a Piezoelectric Actuator," NASA Technical Report NACA/CR-2000-209861, 2000.
- Kellogg, R. and Flatau, A.B. 1999. Blocked Force Investigation of a Terfenol-D Transducer," *SPIE 6th International Symposium on Smart Structures and Materials*, March 1999, Paper No. 3668-19.
- Kellogg, R. and Flatau, A.B. 2001. "Investigation of a Terfenol-D Tunable Mechanical Resonator," In: *Proceedings of SPIE*, Vol. 4327, pp. 550–559.
- Kessler, H. and Balke, H. 2001. "On the Local and Average Energy Release in Polarization Switching Phenomena," *Journal of the Mechanics and Physics of Solids*, 49(5):953–978.
- Krueger, H.H.A. 1967. "Stress Sensitivity of Piezoelectric Ceramics: Part 1. Sensitivity to Compressive Stress Parallel to the Polar Axis," *The Journal of the Acoustical Society of America*, 42(3):636–645.
- Krueger, H.H.A. 1968. "Stress Sensitivity of Piezoelectric Ceramics: Part 3. Sensitivity to Compressive Stress Perpendicular to the Polar Axis," *Journal of the Acoustical Society of America*, 43(3):583–591.
- Krueger, H.H.A. and Berlincourt, D. 1961. "Effects of High Static Stress on the Piezoelectric Properties of Transducer Materials," *The Journal of the Acoustical Society of America*, 33(10):1339–1344.
- Lee, T. and Chopra, I. 1999. "Development and Validation of a Refined Piezostack-Actuated Trailing Edge Flap Actuator for a Helicopter Rotor," In: *Proceedings on SPIE Conference on Smart Structures and Integrated Systems*, Newport Beach, CA, Vol. 3668, pp. 22–36.
- Liang, C., Sun, F.P. and Rogers, C.A. 1994. "Coupled Electro-Mechanical Analysis of Adaptive Material Systems – Determination of the Actuator Power Consumption and System Energy Transfer," *Journal of Intelligent Material Systems and Structures*, 5(1):12–20.
- Lin, C.-Y. and Hagood, N.W. 2000. "Compression Depolarization of PZT Piezoelectric Materials under High Electromechanical Driving Levels," *Proceedings SPIE Conference on Smart Structures and Materials*, Newport Beach, CA, Vol. 3992, pp. 115–125.
- Lynch, C.S. 1996. "The Effect of Uniaxial Stress on the Electro-Mechanical Response of 8/65/35 PLZT," *Acta Materialia*, 44(10):4137–4148.
- Maxwell, J.K. 1891. *A Treatise on Electricity & Magnetism*, Vol.1, Dover Publications, Inc., 1954.
- Mitrovic, M., Carman, G.P. and Straub, F.K. 2000. "Durability Characterization of Piezoelectric Stack Actuators under Combined Electro-Mechanical Loading," *41st AIAA/ASME/ASCE/AHS/ASC Conference Structures, Structural Dynamics, and Materials*, Atlanta, GA, Paper No. AIAA 2000-1500.
- Mitrovic, M., Carman, G.P., and Straub, F.K. 2001. "Response of Piezoelectric Actuators under Combined Electromechanical Loading," *International Journal of Solids and Structures*, 38(24–25):4357–4374.
- Pan, M.-J., Rehrig, P.W., Kucera, J.P., Park, S.-E. and Hackenberger, W.S. 2000. "Comparison of Actuator Properties for Piezoelectric and Electrostrictive Materials," In: *Proceedings SPIE Conference on Smart Structures and Materials*, Newport Beach, CA, Vol. 3992, pp. 80–90.
- Pomirleanu August 2001. "Induced Strain Actuators for Smart-Structures Applications," M.S. Thesis, University of South Carolina, Mechanical Engineering Department, Columbia SC.
- Pratt, J.R., Oueini, S.S. and Nayfeh, A.H. 1999. "Terfenol-D Nonlinear Vibration Absorber," *Journal of Intelligent Materials Systems and Structures*, 10(1):29–35.
- Sirohi, J. and Chopra, I. 2000. "Fundamental Behavior of Piezoceramic Sheet Actuators," *Journal of the Intelligent Material Systems and Structures*, 11(1):47–61.
- Smith, R.C. 1998. "A Nonlinear Physics-Based Optimal Control Method for Magnetostrictive Actuators," ICASE Report No. 98-4.
- Straub, F.K. and Merkley, D.J. 1995. "Design of a Smart Material Actuator for Rotor Control," *1995 SPIE North American Conference on Smart Structures and Materials, Smart Structures and Integrated Systems*, San Diego, CA, Paper No. 2443-10.
- Straub, F.K., Ngo, H.T., Anand, V. and Domzalski, D.B. 2001. "Development of a Piezoelectric Actuator for Trailing Edge Flap Control of Full-Scale Rotor Blades," *Smart Materials and Structures*, 10(1):25–34.
- Uchino, K., 2000. *Ferroelectric Devices*, Marcel Dekker Inc., New York.
- Yang, G., Liu, S.-F., Ren, W. and Mukjerjee, B.K. 2000. "Uniaxial Stress Dependence of the Piezoelectric Properties of Lead Zirconate Titanate Ceramics," In: *Proceedings on SPIE Conference on Smart Structures and Materials 2000: Active Materials: Behavior and Mechanics*, Newport Beach, CA, Vol. 3992, pp. 103–113.



Yoshikawa, S., Farrell, M., Warkentin, D., Jacques, R. and Saarmaa, E. 1999. "Monolithic Piezoelectric Actuators and Vibration Dampers with Interdigital Electrodes," In: *Proceedings on SPIE Conference on Smart Structures and Materials* 1999, Newport Beach, CA, Vol. 3668, pp. 578–585.

Zhang, Q.M., Zhao, J., Uchino, K. and Zheng, J. 1997. "Change of Weak-field Properties of  $\text{Pb}(\text{ZrTi})\text{O}_3$  Piezoceramics with Compressive Uniaxial Stresses and its Links to the Effect of Dopants on the Stability of the Polarizations in the Materials," *Journal of Material Research*, 12(1):226–234.

